Publ. Astron. Soc. Japan (2019) 71 (2), 27 (1–18)
doi: 10.1093/pasj/psy145
Advance Access Publication Date: 2019 January 7

Star formation and polycyclic aromatic hydrocarbons in ELAIS N1 galaxies as seen by AKARI

Tímea O. Kovács,[1,*] Denis Burgarella,[2] Hidehiro Kaneda,[3] Dániel Cs. Molnár,[4,5] Shinki Oyabu,[3] Sandor Pinter,[1] and L. Viktor Toth[1,6]

[1]Department of Astronomy, Eötvös Loránd University, Pázmány Péter sétány 1/A, H-1117 Budapest, Hungary
[2]Aix-Marseille Université, CNRS, Laboratoire d'Astrophysique de Marseille, UMR 7326, 13388 Marseille, France
[3]Graduate School of Science, Nagoya University, Furo-cho, Chikusa-ku, Nagoya, Aichi 464-8602, Japan
[4]Astronomy Centre, Department of Physics and Astronomy, University of Sussex, Brighton, BN1 9QH, UK
[5]INAF – Osservatorio Astronomico di Cagliari, Via della Scienza 5, I-09047 Selargius (CA), Italy
[6]Konkoly Observatory of the Hungarian Academy of Sciences, H-1121 Budapest, Konkoly Thege Miklós út 15-17, Hungary

*E-mail: timea.kovacs95@gmail.com

Received 2018 August 26; Accepted 2018 November 25

Abstract

We have examined the relationship between star formation and polycyclic aromatic hydrocarbons (PAHs) in a variety of galaxies. PAHs are excited by the ultraviolet photons of young stars, but they are disassociated by strong UV radiation in starbursts. Therefore their emission (which is in the wavelength range covered by AKARI) can be used as a star formation tracer in main sequence galaxies. We selected our targets in the ELAIS N1 field with AKARI detections, matched them with the Herschel Point Source Catalog, and collected other publicly available photometric data. Their spectral energy distributions (SEDs) were fitted, and several parameters of the galaxies were estimated, e.g., star formation rate (*SFR*), stellar mass, and the fraction of PAHs compared to dust mass ($q_{\rm PAH}$), and we examined the relationships between these parameters. The final sample consisted of 48 galaxies, with redshifts from 0.04 to 2.36. The estimated $q_{\rm PAH}$ values were lower on average than typical values in the literature. This could be due to various reasons, such as low metallicity, or ongoing active galactic nucleus or starburst activity. Of our sample, 83% of the objects fell in the star-forming main sequence of galaxies, while only 8% could be considered as starbursts. We found a decreasing $q_{\rm PAH}$ trend with increasing $A_{\rm V}$ and consequently $L_{\rm IR}$, suggesting the possible presence of compact star-forming regions. We compared the $q_{\rm PAH}$ values with the known relations of the PAH luminosities, but they did not always follow the same trends (*SFR*, $L_{\rm IR}$), and showed only slight correlation with the PAH luminosities.

© The Author(s) 2019. Published by Oxford University Press on behalf of the Astronomical Society of Japan.
All rights reserved. For permissions, please e-mail: journals.permissions@oup.com

Downloaded from https://academic.oup.com/pasj/article-abstract/71/2/27/5274622 by The Library of Chinese Academy of Sciences user on 02 August 2019

Key words: galaxies: ISM — galaxies: star formation — infrared: galaxies

1 Introduction

ELAIS (European Large Area ISO Survey) was one of the biggest open-time projects of the Infrared Space Observatory (ISO: Rowan-Robinson et al. 1999). Measurements were taken in four dlargeabsifferent bands (in a wavelength range of 6.7–175 μm) of multiple regions on the sky (12 square degrees in total). They took into account several considerations when choosing these areas. All of the regions are at large ecliptic latitudes ($|\beta| > 40^\circ$) to minimize the effects of zodiacal light, and they also avoided areas with bright 100 μm and 12 μm emission. One of these regions was the ELAIS N1 field ($\alpha = 16^{\rm h}10^{\rm m}1^{\rm s}$, $\delta = +54^\circ30'36''$; Oliver et al. 2000). Multiple follow-up surveys were carried out in different wavelength regimes, from the optical to radio, including spectroscopic measurements. In this way the ELAIS N1 field became one of the most well-studied regions on the sky. Due to its rich ancillary data set, ELAIS N1 is thus an ideal field for galaxy evolution studies.

Beside the AKARI all-sky survey, there is also an AKARI deep field observation dedicated to this field. AKARI made measurements in the mid- and far-infrared, including data in the wavelength regime that probes, for example, polycyclic aromatic hydrocarbon (PAH) emissions.

PAHs are the smallest dust grains found in interstellar matter. Their emissions mostly come from photodissociation regions (PDRs). They have broad emission features at 3.3, 6.2, 7.7, 8.6, 11.3, 12.7, and 17 μm caused by vibrational transitions (e.g., Tielens 2008). PAHs can be used as star formation rate (*SFR*) tracers (Brandl et al. 2006), because they are excited by ultraviolet (UV) light from young stars, and emit their energy at longer wavelengths, in the mid-infrared. Their emissions also correlate with the infrared luminosity ($L_{\rm IR}$; Caputi et al. 2007), which also indicates star formation shrouded by dust. The relation between PAH emission and *SFR* is more complex, because PAHs can be destroyed by strong radiation caused by active galactic nuclei (AGNs: Weedman et al. 2005) or starbursts. The stellar far-UV (FUV) flux can also be absorbed by dust in H II regions so it does not reach the PAHs in PDRs, causing lower PAH emission (Peeters et al. 2004; Tielens 2008). Hence galaxies with extreme star formation or an AGN can have a deficiency in PAH emission.

A possible approach to identifing starburst galaxies is to examine their location in the *SFR*–stellar mass (M_*) plane, where most normal star-forming galaxies at a given redshift form a tight relation known as the star-forming main sequence (MS: Noeske et al. 2007). According to the observed trends, the *SFR* of galaxies increases at higher stellar mass and redshift. Galaxies below the MS are thought to be quiescent, passive objects, with little or no ongoing star formation, and galaxies above the MS are starbursts. The precise shape and properties of the MS are still matters of debate. In this paper we adopt the commonly used definition of Schreiber et al. (2015). They used Herschel measurements and determined an MS valid up to $z = 4$. According to them, the star formation rate of MS galaxies can be expressed as

$$\log(SFR_{\rm MS}) = m - m_0 + a_0 r - a_1[\max(0, m - m_1 - a_2 r)]^2, \quad (1)$$

where $m = \log(M_*/10^9\,M_\odot)$, $r = \log(1+z)$, and m_0, m_1, a_0, a_1, a_2 are different constants.

Another way of examining the mode of star formation is by looking at the specific star formation rate, defined as the *SFR* per unit mass ($sSFR = SFR/M_*$). The *sSFR* of the main sequence increases with redshift:

$$sSFR_{\rm MS}\,[{\rm Gyr}^{-1}] = 26 \cdot t_{\rm cosmic}^{-2.2}, \quad (2)$$

where $t_{\rm cosmic}$ is the age of the Universe at the given redshift in gigayears (Elbaz et al. 2011). The "starburstiness" of a galaxy can be defined as

$$R_{\rm SB} = sSFR/sSFR_{\rm MS}. \quad (3)$$

An $R_{\rm SB}$ between 1/4 and 4 signals regular star formation, with values below indicating a quiescent galaxy, and values above showing signs of a starburst phase (Rodighiero et al. 2011; Sargent et al. 2012).

To test the relationship between PAHs and star formation, we collected photometric data for galaxies in the ELAIS N1 field. We included Herschel data to get a better estimate of the star formation rate, and AKARI data for a better constraint on the PAH luminosity.

2 Input data

2.1 AKARI photometric catalogs

The AKARI infrared space observatory (Murakami et al. 2007) was launched on 2006 February 21 and was operational until 2011 November 24. One of the main missions of AKARI was to carry out the All-Sky Survey with the Far Infrared Surveyor and the Infrared Camera (IRC: Onaka

Downloaded from https://academic.oup.com/pasj/article-abstract/71/2/27/5274622 by The Library of Chinese Academy of Sciences user on 02 August 2019

et al. 2007). The IRC scanned more than 90% of the entire sky at two mid-infrared bands with effective wavelengths at 9 and 18 μm during the cryogenic mission phase (Ishihara et al. 2010). There are two AKARI catalogs available on the ELAIS N1 field in the mid-infrared: the AKARI AKARI/IRC All-Sky Survey Point Source Catalog Version 1.0 (Ishihara et al. 2010), and the AKARI/IRC source catalogs and source counts for the IRAC Dark Field, ELAIS North, and the AKARI Deep Field South (Davidge et al. 2017). Unfortunately there are very few sources in the ELAIS N1 field in the first catalog: 16 in a, area of 2 square degrees. Five of those 16 sources have photometric redshifts.

Davidge et al. (2017) developed a new optimized analysis toolkit specifically for processing AKARI deep field images, to extract extragalactic point sources better than the original pipeline. This toolkit was applied to three extragalactic survey fields. ELAIS N1 was one of them, and the field (centered at RA = $16^{h}10^{m}1^{s}$, Dec = $+54^{\circ}57'00''$ J2000.0) was observed as part of the FU-HYU (Follow-Up Hayai-Yasui Umai, PI: C. Pearson) AKARI Mission Program. It is one of the deepest surveys performed by AKARI, but the survey area is only 0.028 square degrees. Fluxes are available at 4.1, 11, 15, and 18 μm, but most of the sources only have a detection at 4.1 μm.

2.2 The Herschel Point Source Catalogs

The Herschel space telescope made observations in the far-infrared (70–500 μm; Pilbratt et al. 2010). Recently, point source catalogs were released for both Herschel PACS and SPIRE, and these were also used in our analysis. Fluxes in the PACS Point Source Catalog (Marton et al. 2017) were determined by aperture photometry on intensity maps, while the SPIRE Point Source Catalog (Schulz et al. 2017) fluxes were determined with the timeline fitter on timeline data. First we matched our sources to these catalogs, but we found only 31 sources with SPIRE fluxes. To also include fainter far-infrared (FIR) objects, we determined SPIRE fluxes ourselves in the AKARI deep field using the Sussextractor routine of HIPE (Herschel Science Ground Segment Consortium 2011).

2.3 Other data

We also used the public archives of further all-sky surveys like SDSS (Blanton et al. 2017), WISE (Cutri et al. 2014), and photometry from region-specific catalogs, like IRAC/MIPS from Rowan-Robinson et al. (2013). Radio catalogs—Pi GHz Sky Survey III: ELAIS-N1, Coma, and Lockman fields (Croft et al. 2013) at 3.04 and 3.14 GHz; DRAO ELAIS N1 catalog (Grant et al. 2010) at 1.4 GHz—were also checked, but there were no matches to our final source list. For galaxies without SDSS data, we used the collected optical photometry from Rowan-Robinson et al. (2013).

2.4 Source selection

We selected sources with detections of at least one of the 11, 15, or 18 μm AKARI IRC bands, and at least one Herschel detection. The AKARI data constrains the PAH, and the Herschel data constrains the FIR emission (caused by larger dust grains). We found 64 such sources in total, as listed in table 1) with their catalog number in the Davidge et al. (2017) catalog, their SIMBAD identification, and their (J2000.0) equatorial coordinates. The collected photometry can be seen in the Appendix in tables 6–10.

We obtained redshifts for the galaxies from SDSS DR14 (Abolfathi et al. 2018) and from the survey of Rowan-Robinson et al. (2013). Only 14 galaxies had spectroscopic redshifts, for which the mean error was 10^{-4}. The other 50 galaxies had only photometric redshifts available, with a mean error of 0.1. We used the redshifts from SDSS DR14, except for those objects which only had redshifts in Rowan-Robinson et al. (2013).

The redshift range of the sample was relatively wide, spanning from $z = 0.04$ up to $z = 4.5$, and 28 of the sources had a redshift above 0.5. A histogram of the redshift distribution is shown in figure 1.

3 SED fitting

We used version 0.11.0 of the CIGALE (Code Investigating GALaxy Emission; Burgarella et al. 2005; Noll et al. 2009; Boquien et al. 2018) software package to model the spectral energy distributions (SEDs) of the galaxies. The code is highly flexible, providing multiple different models for each physical process or component (e.g., stellar and dust emission, attenuation, etc.), and it works over a large wavelength range, from UV to radio. The attenuation and dust emission modules are connected by an energy balance (the amount of energy absorbed by the dust in UV is equal to the energy emitted at IR wavelengths). The program finds the best-fit SED by χ^2 minimization, and computes the physical parameters of galaxies by Bayesian analysis, as described in Noll et al. (2009).

We applied the following modules for our CIGALE fits: a delayed τ model for star formation history, the Bruzual and Charlot (2003) stellar emission model with Chabrier (2003) initial mass function, the nebular module (lines and continuum emission), a double power-law attenuation curve (combining the attenuation caused by the warmer birth clouds and the cold interstellar medium), with the updated Draine and Li (2007) infrared model.

Downloaded from https://academic.oup.com/pasj/article-abstract/71/2/27/5274622 by The Library of Chinese Academy of Sciences user on 02 August 2019

Table 1. The objects examined, with their IDs based on the catalog of Davidge et al. (2017) and their SIMBAD identifier, where available.

ID	SIMBAD ID	RA	Dec
5	[RLP2006] EN1-J160909+550051	242.29054	55.014275
17	[RLP2006] EN1-J160849+545957	242.20709	54.999611
19	[RLP2006] EN1-J160851+550000	242.21466	55.000515
23	[RLP2006] EN1-J160903+545958	242.26601	54.999691
24	[RLP2006] EN1-J160905+545939	242.2718	54.994789
25	[RLP2006] EN1-J160847+545953	242.19643	54.9981
47	[RLP2006] EN1-J160856+545914	242.23463	54.987263
63	[RLP2006] EN1-J160844+545846	242.18674	54.979485
67	[RLP2006] EN1-J160927+545847	242.36244	54.97979
68	[RLP2006] EN1-J160926+545835	242.36099	54.976795
87	[RLP2006] EN1-J160849+545827	242.20818	54.974186
108	[RLP2006] EN1-J160903+545804	242.26262	54.96817
111	[RLP2006] EN1-J160841+545801	242.17259	54.967339
113	[RLP2006] EN1-J160845+545802	242.19052	54.966846
128	[RLP2006] EN1-J160909+545716	242.29112	54.954685
140	[SES2007] DXS3-11	242.26373	54.956341
143	[RLP2006] EN1-J160927+545747	242.3624	54.963287
144	[RLP2006] EN1-J160918+545745	242.32584	54.962498
156	[RLP2006] EN1-J160839+545721	242.16467	54.956055
181	[RLP2006] EN1-J160932+545702	242.38338	54.950798
186	[RLP2006] EN1-J160915+545700	242.31619	54.950207
191	[RLP2006] EN1-J160832+545654	242.13504	54.948326
195	[RLP2006] EN1-J160840+545643	242.17113	54.945126
200	[RLP2006] EN1-J160856+545637	242.23703	54.944157
215	—	242.11346	54.940094
222	[RLP2006] EN1-J160931+545629	242.38307	54.941467
261	[RLP2006] EN1-J160918+545544	242.3287	54.929192
264	[RLP2006] EN1-J160935+545541	242.39844	54.928429
266	[RLP2006] EN1-J160850+545547	242.21262	54.930222
286	[RLP2006] EN1-J160929+545511	242.3744	54.91975
289	[RLP2006] EN1-J160839+545523	242.16547	54.922676
294	2MASS J16083353+5455097	242.13895	54.919468
300	ELAISC15 J160828+545506	242.11836	54.919254
305	[RLP2006] EN1-J160851+545501	242.21483	54.917511
329	[RLP2006] EN1-J160857+545445	242.23959	54.912827
334	[DLM2005] FN1 25S	242.14328	54.905727
347	[RLP2006] EN1-J160909+545435	242.28891	54.90992
365	—	242.11362	54.904194
370	—	242.10393	54.904659
385	[RLP2006] EN1-J160918+545351	242.32613	54.897442
412	—	242.14195	54.893471
416	[RLP2006] EN1-J160859+545333	242.2495	54.892723
417	[RLP2006] EN1-J160859+545327	242.24692	54.891033
419	[RLP2006] EN1-J160912+545326	242.30347	54.890713
433	[RLP2006] EN1-J160845+545302	242.18961	54.884129
438	[RLP2006] EN1-J160907+545311	242.28104	54.886497
447	[RLP2006] EN1-J160840+545257	242.16656	54.883514
456	[RLP2006] EN1-J160850+545252	242.21201	54.881504
490	[RLP2006] EN1-J160902+545207	242.2589	54.868843
500	[RLP2006] EN1-J160848+545150	242.20291	54.863754
531	[RLP2006] EN1-J160857+545053	242.24165	54.848621
545	[RLP2006] EN1-J160910+545024	242.29269	54.84024
554	[RLP2006] EN1-J160904+550126	242.26964	55.02475
555	ELAISC15 J160855+550109	242.23241	55.020046
559	[RLP2006] EN1-J160915+550027	242.31432	55.007153
562	[RLP2006] EN1-J160926+545835	242.36111	54.978039
565	[RLP2006] EN1-J160911+545727	242.29738	54.958267
568	[RLP2006] EN1-J160843+545557	242.17867	54.932854
570	[RLP2006] EN1-J160931+545526	242.3793	54.924835
574	[RLP2006] EN1-J160853+550056	242.22147	55.015846
580	[RLP2006] EN1-J160909+545814	242.28893	54.971088
590	[RLP2006] EN1-J160906+545007	242.27696	54.834644
591	[RLP2006] EN1-J160854+550159	242.2267	55.033611
597	[RLP2006] EN1-J160843+550015	242.18056	55.004337

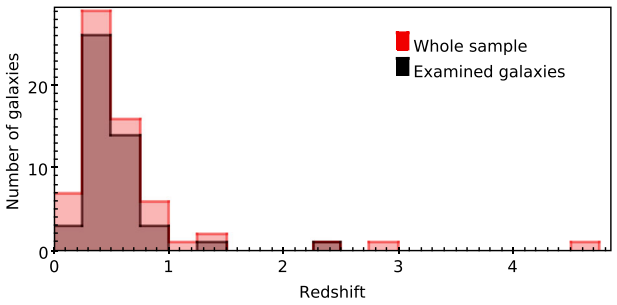


Fig. 1. Redshift distribution of the original sample of 64 galaxies, and the distribution of the 48 sources which have a good SED fit, whose parameters were examined; 28 of the sources had a redshift above 0.5, and from these 19 had a good SED fit. (Color online)

Table 2. Parameters from the Draine and Li (2007) dust model, and the ranges used in the SED fitting.

Parameter	Range
$q_{\rm PAH}$	0.47–7.32
$U_{\rm min}$	0.1–30
$U_{\rm max}$	10^7
α	1–3
γ	0.01–0.5

Regarding the estimation of the *SFR*, and the contribution of the PAHs, the most important module is the dust module. The Draine and Li (2007) model provides multiple tunable parameters: $U_{\rm min}$ and $U_{\rm max}$ are dimensionless scaling factors, and correspond to the minimum and maximum radiation intensity of the starlight (the energy density per unit frequency is given by $u_\nu = U u^{\rm MMP83}$, where $u^{\rm MMP83}$ is the interstellar radiation field for the solar neighbourhood; Mathis et al. 1983). Part of the dust is heated by the minimum radiation intensity ($U_{\rm min}$), and another part is heated by a distribution of intensities from $U_{\rm min}$ to $U_{\rm max}$. α is the power-law slope of $dU/dM \sim U^\alpha$, and γ is the PDR contribution: the part of the dust heated by the radiation distribution. $1-\gamma$ is the contribution of the general diffuse ISM, heated by $U_{\rm min}$.

Our main parameter of interest was the PAH fraction of the total dust mass ($q_{\rm PAH}$). In the updated Draine and Li models (implemented in Cigale: Aniano et al. 2012; Ciesla et al. 2014) it can vary from 0.47% up to 7.32%. The parameter ranges chosen in the dust module are given in table 2 ($U_{\rm max}$ cannot be changed in the updated module, it is fixed at 10^7).

The SED fitting results are listed in table 3, where the columns are (1) Davidge catalog number; (2) redshift; (3) total stellar mass; (4) luminosity; (5) *SFR*; (6) dust mass; (7) $q_{\rm PAH}$; (8) $R_{\rm SB}$. Sample SED fits are shown in figures 2 and 3. The SEDs were also fitted with and without AKARI data.

Downloaded from https://academic.oup.com/pasj/article-abstract/71/2/27/5274622 by The Library of Chinese Academy of Sciences user on 02 August 2019

Table 3. Derived parameters from the SED fitting.

ID[†]	z	$\log M_*$ ($M_\odot$)	$\log L_{IR}$ ($L_\odot$)	SFR ($M_\odot$ yr^{-1})	$\log M_{\rm d}$ ($M_\odot$)	$q_{\rm PAH}$ (%)	$R_{\rm SB}$
17	0.41	10.27 ± 0.1	10.88 ± 0.12	5.2 ± 1.91	8.24 ± 0.53	1.39 ± 0.56	1.44
23	0.35	11.01 ± 0.03	10.74 ± 0.02	0.27 ± 0.18	9.5 ± 0.02	1.12 ± 0.06	0.02
24	0.43	10.56 ± 0.11	11.08 ± 0.14	7.8 ± 3.76	9.0 ± 0.33	0.87 ± 0.36	1.07
25	0.36	10.57 ± 0.07	10.73 ± 0.13	4.27 ± 1.63	8.99 ± 0.28	4.15 ± 1.52	0.66
63	0.04	8.63 ± 0.07	8.88 ± 0.02	0.11 ± 0.01	6.47 ± 0.07	1.77 ± 0.09	2.91
68	0.48	10.23 ± 0.13	11.48 ± 0.03	25.92 ± 5.17	8.46 ± 0.15	0.47 ± 0.02	7.04
87	0.51	10.36 ± 0.07	11.21 ± 0.04	14.55 ± 1.65	9.97 ± 0.04	2.09 ± 0.39	2.73
108	0.67	10.94 ± 0.06	11.3 ± 0.13	17.14 ± 6.1	9.63 ± 0.09	0.47 ± 0.04	0.64
111	0.48	10.26 ± 0.07	11.09 ± 0.08	10.55 ± 2.22	9.08 ± 0.32	1.2 ± 0.22	2.68
113	0.51	10.54 ± 0.08	11.0 ± 0.19	8.64 ± 4.21	8.92 ± 0.45	3.79 ± 1.47	1.08
128	0.48	10.69 ± 0.07	11.07 ± 0.08	7.8 ± 2.51	9.36 ± 0.32	1.11 ± 0.06	0.73
143	0.37	10.66 ± 0.07	10.85 ± 0.04	2.88 ± 0.86	8.73 ± 0.25	1.83 ± 0.24	0.35
144	0.43	10.68 ± 0.08	10.75 ± 0.3	3.81 ± 4.16	8.2 ± 0.43	1.17 ± 0.61	0.4
156	0.55	11.29 ± 0.08	11.5 ± 0.13	12.6 ± 7.8	8.31 ± 0.59	1.62 ± 0.54	0.26
181	0.41	10.07 ± 0.08	10.95 ± 0.03	7.31 ± 0.87	9.71 ± 0.03	1.29 ± 0.29	3.27
186	2.36	11.52 ± 0.03	12.5 ± 0.06	263.2 ± 42.8	10.11 ± 0.62	2.23 ± 1.09	0.29
191	1.43	10.79 ± 0.07	12.09 ± 0.11	111.68 ± 35.63	10.31 ± 0.44	2.32 ± 0.98	1.91
195	0.59	11.43 ± 0.04	11.17 ± 0.11	3.31 ± 0.67	9.57 ± 0.28	3.88 ± 0.94	0.05
200	0.53	10.95 ± 0.06	11.34 ± 0.1	12.73 ± 4.91	9.74 ± 0.19	1.5 ± 0.34	0.6
222	0.39	10.02 ± 0.08	10.83 ± 0.15	6.5 ± 2.74	9.19 ± 0.26	1.35 ± 0.45	3.34
261	0.61	10.91 ± 0.04	11.84 ± 0.06	55.1 ± 7.63	8.53 ± 0.51	1.11 ± 0.08	2.46
264	0.29	10.41 ± 0.09	10.68 ± 0.13	2.22 ± 1.31	8.03 ± 0.35	1.63 ± 0.33	0.56
286	0.37	10.64 ± 0.06	10.94 ± 0.07	4.62 ± 1.24	8.95 ± 0.29	3.23 ± 0.79	0.59
289	0.34	10.64 ± 0.09	11.11 ± 0.05	9.19 ± 1.49	8.31 ± 0.23	3.62 ± 0.65	1.26
294	0.05	9.84 ± 0.03	9.74 ± 0.02	0.66 ± 0.13	7.56 ± 0.02	3.96 ± 0.2	1.05
300	0.91	10.78 ± 0.08	12.11 ± 0.12	115.46 ± 35.12	9.11 ± 0.67	1.77 ± 1.07	4.16
329	0.84	10.57 ± 0.06	11.54 ± 0.04	28.64 ± 4.01	10.33 ± 0.04	1.67 ± 0.3	1.87
334	0.11	9.94 ± 0.06	10.29 ± 0.03	2.61 ± 0.2	8.08 ± 0.07	3.18 ± 0.26	2.87
416	0.51	10.59 ± 0.06	11.2 ± 0.07	10.78 ± 2.48	8.67 ± 0.5	1.99 ± 0.48	1.21
417	0.51	10.84 ± 0.06	11.16 ± 0.05	7.07 ± 2.27	9.12 ± 0.24	1.36 ± 0.44	0.45
419	0.63	10.92 ± 0.07	11.72 ± 0.14	41.06 ± 16.54	9.23 ± 0.29	0.68 ± 0.31	1.71
433	0.69	10.27 ± 0.15	11.27 ± 0.13	14.93 ± 6.55	9.8 ± 0.2	2.17 ± 0.64	2.55
438	0.45	10.52 ± 0.1	10.91 ± 0.03	5.87 ± 1.12	9.67 ± 0.03	1.13 ± 0.1	0.86
447	0.45	10.18 ± 0.09	10.86 ± 0.11	6.41 ± 1.85	8.47 ± 0.51	2.32 ± 0.88	2.04
456	0.41	10.25 ± 0.11	10.71 ± 0.18	4.04 ± 1.96	9.07 ± 0.28	2.55 ± 1.34	1.2
490	0.93	10.21 ± 0.02	11.39 ± 0.05	41.19 ± 2.09	9.6 ± 0.38	5.66 ± 0.97	5.38
500	0.26	10.82 ± 0.07	11.4 ± 0.02	15.7 ± 1.07	8.53 ± 0.02	1.77 ± 0.09	1.68
531	0.39	11.0 ± 0.05	10.96 ± 0.06	2.03 ± 1.5	7.95 ± 0.15	1.12 ± 0.06	0.11
554	0.53	10.89 ± 0.08	11.26 ± 0.2	9.8 ± 7.96	9.4 ± 0.26	2.54 ± 1.41	0.53
559	0.4	11.03 ± 0.09	10.92 ± 0.06	2.09 ± 1.76	9.59 ± 0.07	1.99 ± 0.36	0.1
562	0.48	10.24 ± 0.14	11.47 ± 0.06	25.04 ± 5.88	8.48 ± 0.44	0.59 ± 0.25	6.57
565	0.52	10.37 ± 0.07	11.01 ± 0.05	6.41 ± 0.87	9.7 ± 0.14	3.16 ± 0.44	1.17
568	0.46	10.87 ± 0.09	11.31 ± 0.1	12.11 ± 4.91	8.69 ± 0.35	1.02 ± 0.42	0.77
570	0.35	10.53 ± 0.1	10.66 ± 0.14	2.04 ± 1.35	9.15 ± 0.19	1.67 ± 0.49	0.35
574	0.42	10.55 ± 0.09	10.86 ± 0.03	4.59 ± 1.22	9.63 ± 0.03	2.82 ± 0.44	0.66
590	0.29	10.15 ± 0.09	10.55 ± 0.12	3.46 ± 0.82	8.38 ± 0.42	4.03 ± 1.5	1.62
591	0.43	10.76 ± 0.08	10.98 ± 0.1	6.34 ± 2.19	8.6 ± 0.22	0.74 ± 0.33	0.55
597	0.5	10.16 ± 0.18	10.99 ± 0.1	9.54 ± 4.22	8.94 ± 0.35	2.96 ± 1.02	2.88

[†]The IDs of the objects are taken from the AKARI deep field catalog (Davidge et al. 2017).

Downloaded from https://academic.oup.com/pasj/article-abstract/71/2/27/5274622 by The Library of Chinese Academy of Sciences user on 02 August 2019

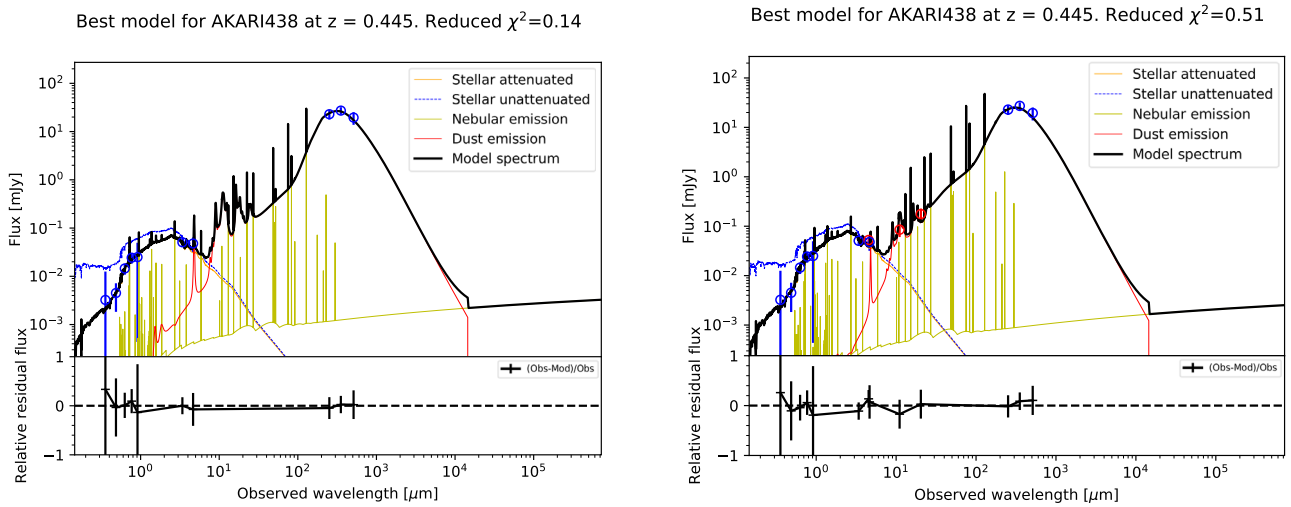


Fig. 2. SED of a galaxy (ID438) with (right) and without (left) AKARI points. Before including the AKARI fluxes, there were no photometric points in the wavelength range of the PAHs. The model spectral energy distribution of the whole galaxy is marked by the solid black line. The unattenuated stellar emission is marked by a dashed blue line, the attenuated by orange, the nebular emission by yellow, and the dust emission by red. The observed fluxes are marked by circles, the red ones showing the added AKARI data. Changes in the SED can be seen at the PAH features, and at longer wavelengths, at 30–60 μm. (Color online)

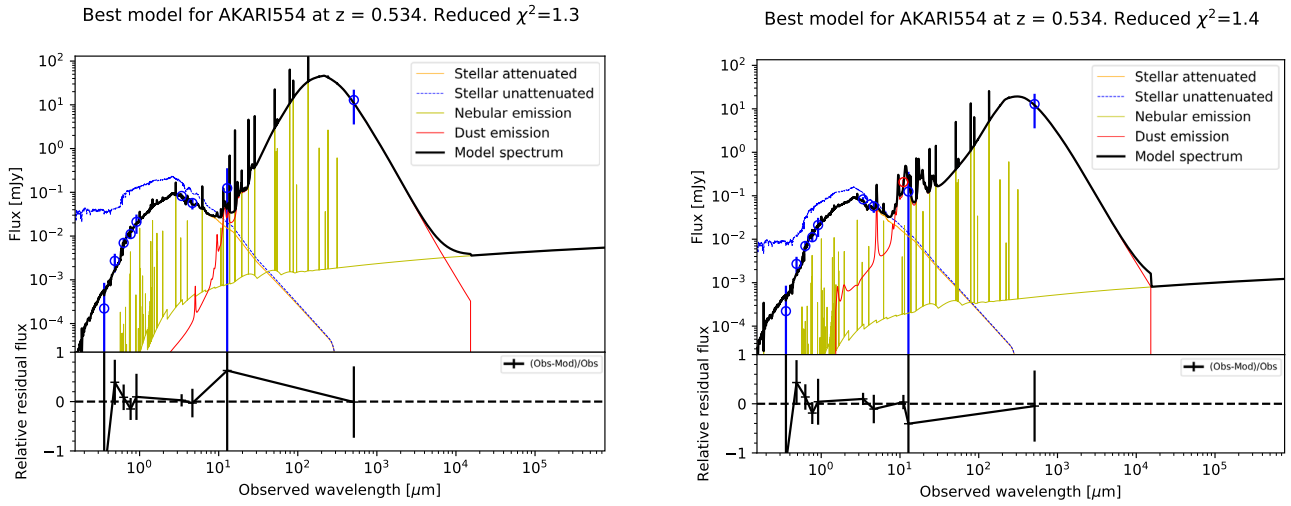


Fig. 3. SED of a galaxy (ID554) with (right) and without (left) AKARI points. Before including the AKARI fluxes, there was only a data point with a large error in the wavelength range of the PAHs. Changes in the SED can be seen at the PAH features, and at the peak of the dust emission. A small difference can also be seen in the UV range. (Color online)

We created a mock catalog with CIGALE (Giovannoli et al. 2011): the code calculates the fluxes of the best-fit model in different filters adding a random error, and fits the SEDs of these simulated objects, calculating the parameters again with a Bayesian-like analysis. By comparing the estimated and the exact values of the mock catalog, we can check the reliability of the different parameters calculated by CIGALE. The comparison for the PAH fraction shows a clear trend (the fitted line is very close to the 1-to-1 line) with a Pearson correlation coefficient of 0.94, as seen in figure 4.

Based on the mock analysis, we conclude that we can estimate this parameter well enough—see further details about using the mock analysis in Ciesla et al. (2014).

4 Results

We examined the parameters of galaxies which had a good SED fit: 48 objects in total (based on the χ^2 statistics—every fit with reduced $\chi^2 \geq 4.5$ was discarded—and based on the mock analysis—every fit with $|q_{\mathrm{PAH,\,estimate}} - q_{\mathrm{PAH,\,best}}| \geq 0.75$ was left out). The results of the SED fittings can

Downloaded from https://academic.oup.com/pasj/article-abstract/71/2/27/5274622 by The Library of Chinese Academy of Sciences user on 02 August 2019

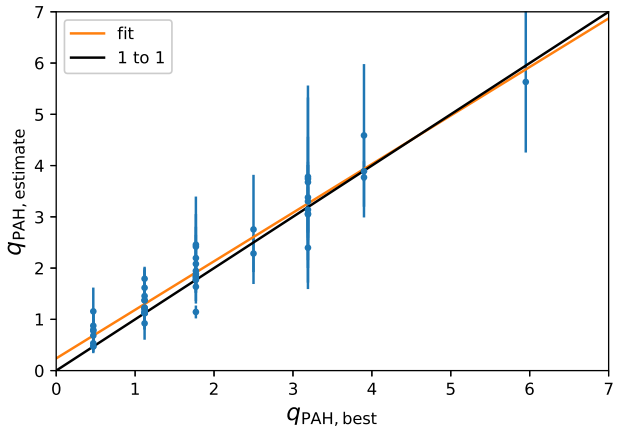


Fig. 4. Result of the mock analysis: the Pearson correlation coefficient is 0.94, and the fitted line is very close to the 1-to-1 line. CIGALE runs the SED fitting on a mock catalog, a simulated catalogue created from the best models of the χ^2 minimization, and calculates the parameters by Bayesian analysis. By comparing the q_{PAH} of the best models (the exact values of the mock SEDs) and the estimated q_{PAH} from the mock analysis, we can determine that the q_{PAH} parameter is estimated correctly by CIGALE. (Color online)

be seen in table 3 (the stellar mass, luminosity, *SFR*, dust mass, and q_{PAH}). All of the selected galaxies have an AKARI measurement at the wavelength of the PAH features.

We investigated the effect of including the AKARI photometric points. Using the AKARI data in the SED fitting improved the error of q_{PAH} on average. It decreased especially in cases where originally the photometry did not include any data at the wavelength of the PAH features (figure 2). The errors of q_{PAH} also got lower, if the galaxy only had photometric points with large errors, for example WISE (figure 3). The mean relative error of q_{PAH} dropped from 37% to 26% with the inclusion of the AKARI photometric points (the different q_{PAH} values are listed in table 4).

The changes of the SED at the PAH wavelengths are shown in figure 5. Including the AKARI data made the PAH emission weaker in some cases (figure 2) and stronger in others (figure 3). The influence of including the AKARI data in the fits is also shown in table 4.

We calculated SFR_{MS} of the galaxies from the Schreiber et al. (2015) main sequence [equation (1)] using their redshifts and stellar masses given by CIGALE. Then we compared them to their *SFR* estimates [$\log(SFR/SFR_{MS})$], and colored them according to their PAH fractions, as seen in figure 6. The criteria for a starburst was $\log(SFR/SFR_{MS}) > 0.5$, and $(SFR/SFR_{MS}) < -0.5$ for a passive galaxy. Nearly the whole sample is star forming (40 sources), or even close to a starburst (4 galaxies). Most of them have relatively low q_{PAH} (2.04 on average). We also fitted the SEDs, and plotted the results of another sample of galaxies in the ELAIS N1 field from Rowan-Robinson et al. (2013) with spectroscopic

Table 4. Estimated q_{PAH} parameters (and errors) before and after including AKARI data.

ID*	Before	After
17	1.66 ± 1.14	1.39 ± 0.56
23	0.5 ± 0.13	1.12 ± 0.06
24	0.53 ± 0.2	0.87 ± 0.36
25	4.95 ± 1.53	4.15 ± 1.52
63	1.64 ± 0.26	1.77 ± 0.09
68	0.47 ± 0.02	0.47 ± 0.02
87	2.29 ± 0.6	2.09 ± 0.39
108	3.69 ± 2.05	0.47 ± 0.04
111	1.04 ± 0.6	1.2 ± 0.22
113	4.07 ± 1.54	3.79 ± 1.47
128	3.01 ± 0.7	1.11 ± 0.06
143	1.56 ± 0.4	1.83 ± 0.24
144	4.63 ± 1.66	1.17 ± 0.61
156	2.98 ± 1.58	1.62 ± 0.54
181	0.55 ± 0.22	1.29 ± 0.29
186	4.05 ± 2.17	2.23 ± 1.09
191	3.88 ± 1.26	2.32 ± 0.98
195	2.79 ± 1.33	3.88 ± 0.94
200	2.12 ± 0.5	1.5 ± 0.34
222	1.96 ± 0.71	1.35 ± 0.45
261	1.08 ± 0.33	1.11 ± 0.08
264	1.13 ± 0.14	1.63 ± 0.33
286	2.56 ± 0.59	3.23 ± 0.79
289	3.54 ± 0.72	3.62 ± 0.65
294	4.41 ± 0.34	3.96 ± 0.2
300	4.03 ± 2.04	1.77 ± 1.07
329	2.17 ± 0.45	1.67 ± 0.3
334	3.44 ± 0.72	3.18 ± 0.26
416	1.08 ± 0.69	1.99 ± 0.48
417	0.64 ± 0.32	1.36 ± 0.44
419	2.21 ± 1.17	0.68 ± 0.31
433	4.72 ± 2.02	2.17 ± 0.64
438	2.61 ± 1.17	1.13 ± 0.1
447	0.79 ± 0.49	2.32 ± 0.88
456	0.73 ± 0.63	2.55 ± 1.34
490	4.57 ± 1.47	5.66 ± 0.97
500	1.77 ± 0.09	1.77 ± 0.09
531	0.49 ± 0.12	1.12 ± 0.06
554	1.64 ± 1.33	2.54 ± 1.41
559	2.58 ± 0.56	1.99 ± 0.36
562	0.47 ± 0.02	0.59 ± 0.25
565	2.04 ± 0.52	3.16 ± 0.44
568	1.04 ± 0.88	1.02 ± 0.42
570	0.59 ± 0.32	1.67 ± 0.49
574	2.45 ± 0.45	2.82 ± 0.44
590	4.04 ± 1.5	4.03 ± 1.5
591	0.52 ± 0.18	0.74 ± 0.33
597	2.76 ± 0.94	2.96 ± 1.02

*The IDs of the objects are taken from the AKARI deep field catalog (Davidge et al. 2017).

Downloaded from https://academic.oup.com/pasj/article-abstract/71/2/27/5274622 by The Library of Chinese Academy of Sciences user on 02 August 2019

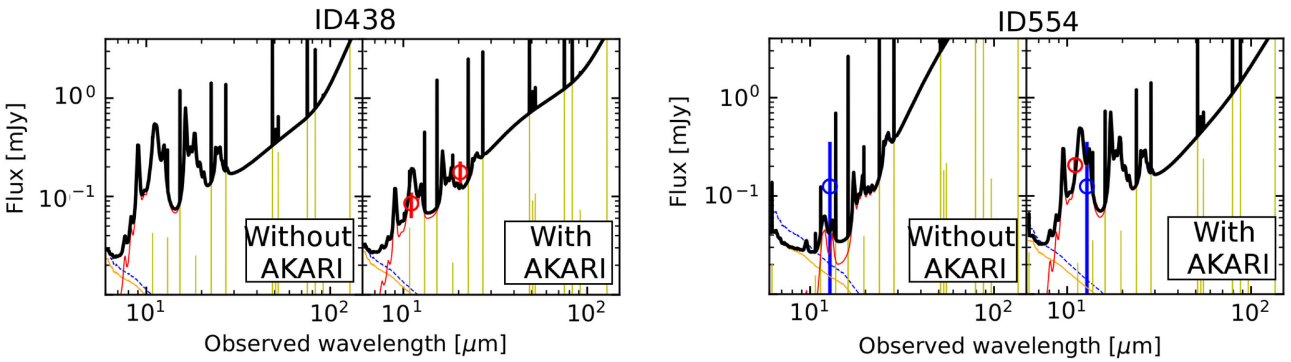


Fig. 5. PAH wavelengths of the two example galaxies (ID438 and ID554), before and after the addition of AKARI data. Left: The galaxy does not have any data at the PAH features before adding the AKARI data. Including the AKARI points (right) made the PAH features less prominent: the $q_{\rm PAH}$ parameter dropped from 2.6% to 1.2%. Other properties of the dust also changed: after including the AKARI data, the γ, α, and dust mass became lower. Right: Before including the AKARI fluxes, there was only a data point with a large error in the wavelength range of the PAHs. With the addition of the AKARI point, the PAH features became more prominent: the $q_{\rm PAH}$ parameter changed from 1.6% to 2.5%, and the dust mass increased. (Color online)

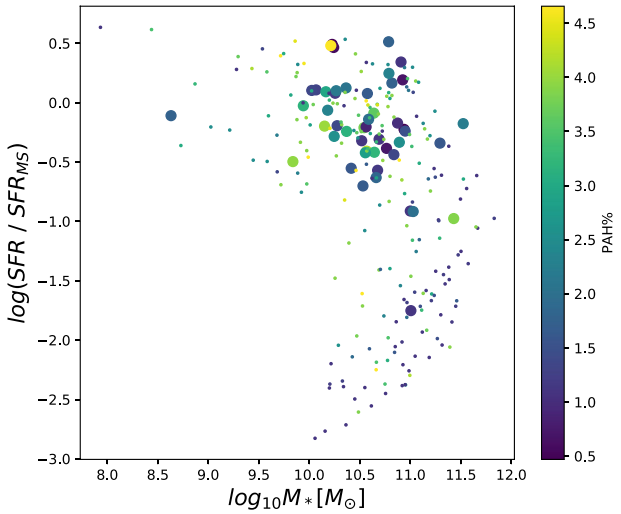


Fig. 6. Logarithmic difference from the main sequence of the examined galaxies as a function of the galaxy stellar mass. The main sequence star formation rate ($SFR_{\rm MS}$) was calculated for each object, from their stellar mass (from CIGALE) and redshift, using equation (1). The points are colored by their $q_{\rm PAH}$ values. The big circles are the galaxies with AKARI data, and the dots are galaxies without AKARI detections. The points split into two groups: a group near the main sequence, and one below it. The AKARI-selected sample consists almost entirely of galaxies around the main sequence. (Color online)

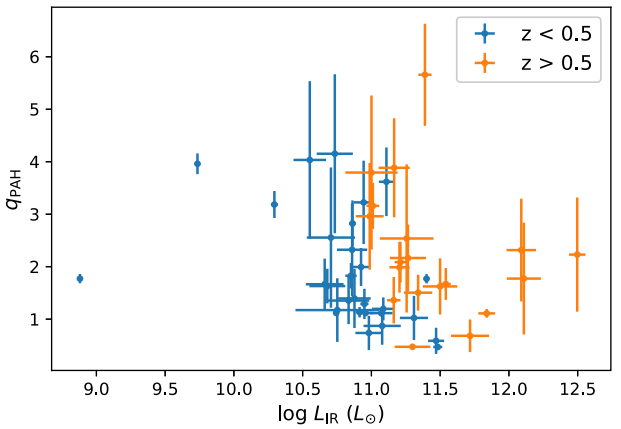


Fig. 7. Value of $q_{\rm PAH}$ compared to the luminosities of galaxies with redshift below and above 0.5. The $q_{\rm PAH}$ parameter seems to drop as the luminosity increases, and after $\log L = 11.5$ increases again in the case of galaxies with $z > 0.5$. (Color online)

redshifts, and no AKARI detections. We used the photometry collected by Rowan-Robinson et al. (2013), and the same catalogs we used for the AKARI-selected sample. These objects show two groups, quiescent and star-forming galaxies, but the AKARI-selected sample contains mostly star-forming galaxies near the main sequence.

$R_{\rm SB}$ was also calculated, from equation (3), using the *sSFR* of the galaxies, and comparing them to the Elbaz et al. (2011) main sequence of equation (2). We found that the majority of the galaxies were star-forming, with $R_{\rm SB}$ between 1/4 and 4. Four galaxies were quiescent, and four were starbursts.

We plotted the PAH fractions of galaxies against their luminosities (figure 7). The PAH fraction drops with increasing luminosities, and it starts to rise in the case of galaxies with higher redshift at higher luminosities ($\log L = 11.5$). This trend is not very significant: the correlation coefficient is -0.51 in the case of low-redshift galaxies, leaving out the galaxies with very low luminosities ($\log L < 10$). The correlation coefficient is even lower (-0.46) at higher redshifts, ignoring objects with very high luminosities ($\log L > 12$). This trend of decreasing $q_{\rm PAH}$ with increasing $L_{\rm IR}$ is similar to the decrease in the ratio of $L_{\rm PAH,\,6.2}/L_{\rm IR}$ as the function of $L_{\rm IR}$ described in Pope et al. (2013). This decreasing trend is possibly attributed to the compactness of the star-forming regions (Pope et al. 2013;

Downloaded from https://academic.oup.com/pasj/article-abstract/71/2/27/5274622 by The Library of Chinese Academy of Sciences user on 02 August 2019

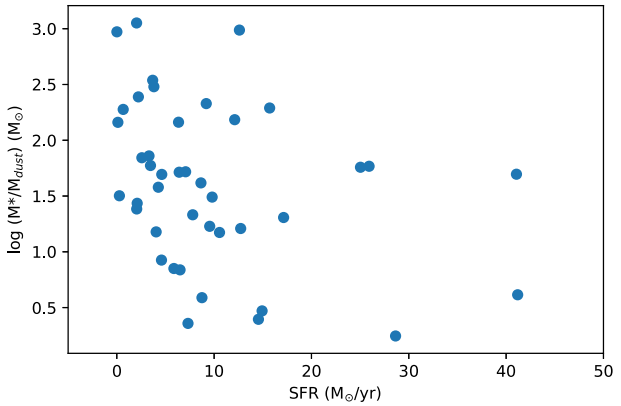


Fig. 8. Stellar to dust mass ratios of the examined galaxies as a function of the star formation rate. No strong relationship between the parameters can be seen in our data, but the *SFR* is slightly decreasing at higher stellar to dust mass ratios. (Color online)

Shipley et al. 2016). $L_{\mathrm{PAH,\,6.2}}/L_{\mathrm{IR}}$ also shows an L_{IR} offset for high-redshift galaxies, similar to what we see in figure 7: galaxies at $z \geq 0.5$ have systematically larger q_{PAH} values for given L_{IR} than galaxies at $z \leq 0.5$, which could imply that there are larger PDRs in higher-redshift galaxies, and larger areas of star formation.

We also examined the relationship between the stellar to dust mass ratio and the *SFR* (figure 8), but no clear relationship can be seen in our data. The *SFR* slightly decreases with a lower stellar to dust mass ratio, but this trend is not significant—the correlation coefficient is only −0.24.

To compare our results to previous studies, we calculated different PAH luminosities from the SEDs and the AKARI fluxes. The 7.7 μm luminosities were calculated for galaxies with different redshifts from the *S11*, *L15*, and *L18* AKARI fluxes. The 6.2, 7.7, and 11.3 μm luminosities and the $\nu L_8/\nu L_{4.5}$ ratios have been calculated from the SEDs.

The SF-AGN classification of sources with spectroscopic data (13 galaxies) were checked in the SDSS database. Three of them were classified as starburst (ID113, ID289, ID555), and two of them as star-forming galaxies (ID25, ID334), but none of them were AGNs. The classification in the SDSS database is based on the Baldwin–Phillips–Terlevich (BPT: Baldwin et al. 1981; Veilleux & Osterbrock 1987) method: the line ratios in H II regions are different from the ones from AGNs. Four of the galaxies that do not have a subclass (ID108, ID261, ID300, ID590) show prominent Hα or Hβ emission; on the other hand there is one galaxy (ID500) with line ratios more typical of AGNs. The starburst galaxies are only slightly above the main sequence based on our SED fitting. The galaxies classified as star forming or showing emission lines are around the main sequence, but one of them can be considered as a starburst galaxy.

Table 5. Value of q_{PAH} from (Schreiber et al. 2018) compared to the results of our sample in different redshift and stellar mass ranges.

z	log M_* ($M_\odot$)	$q_{\mathrm{PAH,\,Sch}}$ (%)	q_{PAH} (%)
0–0.7	9.5–10	3.08	2.73
	10–10.5	4.66	1.91
	10.5–11	3.8	1.84
	11–11.5	6.4	2.15
0.7–1.2	10–10.5	4.73	5.66
	10.5–11	5.47	1.72
1.2–1.8	11–11.5	3.72	2.9
1.8–2.5	11–11.5	2.44	3.1

5 Discussion

We compare the derived q_{PAH} values to previous works, where they determined this parameter with SED fitting. We also compare luminosities derived from our SED fits to papers where different PAH emissions were calculated from AKARI fluxes and spectra, and check whether they follow the same relations as in the literature. We examine whether the q_{PAH} values follow the same trends as the PAH luminosities.

Ciesla et al. (2014) used the same dust module (but only with q_{PAH} up to 4.58%) when they fitted the SEDs of local galaxies ($z = 0$), derived the q_{PAH} values, and examined the relationships of different parameters. They could not find a clear correlation with the *SFR*, only a slight dependency on the stellar mass and metallicity. The average of their q_{PAH} values was 3.87, compared to which our values are much lower on average: 2.04.

Schreiber et al. (2018) stacked galaxies in different redshift and stellar mass ranges, fitted their SEDs, and estimated their PAH fractions. Compared to this work, we also found lower q_{PAH} values on average: the mean q_{PAH} in the different ranges can be found in table 5. Only lower-redshift ($z < 0.5$) galaxies with low stellar mass had similar q_{PAH} to Schreiber et al. (2018). At higher redshifts, the q_{PAH} were sometimes higher, but in that range we only had a few objects.

We also compared our result to articles where the strength of the PAH emissions were examined. Takagi et al. (2010) calculated $\log[\nu L_\nu(7.7\mu\mathrm{m})]$ of $z \sim 1$ galaxies from AKARI fluxes, and compared it with the L_{IR} obtained from SED fitting with the SBURT model. Their results were in good agreement with Houck et al. (2007), who determined a relationship between the two parameters:

$$L_{\mathrm{IR}} = \log[\nu L_\nu(7.7\,\mu\mathrm{m})] + 0.78. \quad (4)$$

Downloaded from https://academic.oup.com/pasj/article-abstract/71/2/27/5274622 by The Library of Chinese Academy of Sciences user on 02 August 2019

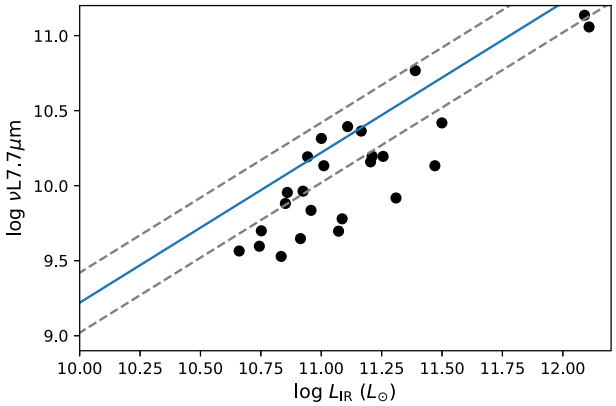


Fig. 9. Comparison between log [$\nu L_\nu(7.7\mu m)$] calculated from the AKARI fluxes and L_{IR} calculated by CIGALE. The solid line is the relation from Houck et al. (2007), and the dashed lines are the 1 σ uncertainties. Our galaxies are slightly below this line. (Color online)

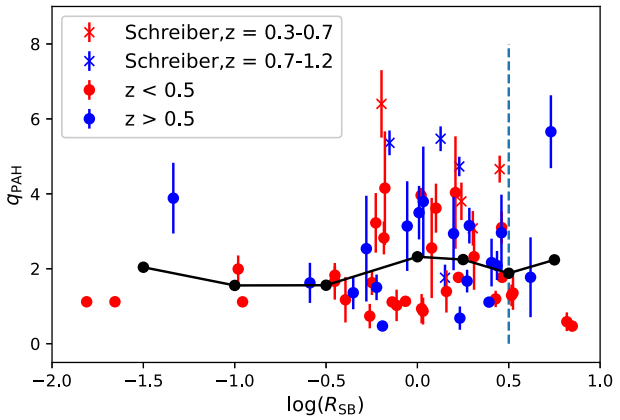


Fig. 10. Value of q_{PAH} as a function of log R_{SB}. The black dots and line show the mean q_{PAH} values in different R_{SB} bins. According to Murata et al. (2014), the $\nu L_8/\nu L_{4.5}$ ratios increase until log $R_{SB} = 0.5$. The q_{PAH} is mostly constant, only seeming to increase slightly at $R_{SB} = 0$. (Color online)

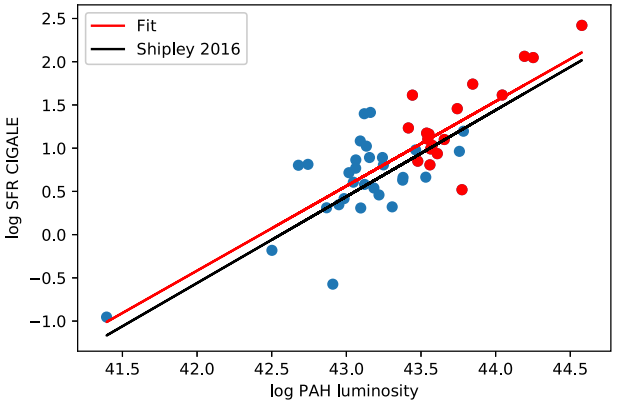


Fig. 11. Comparison between the logarithm of the PAH luminosities of the best-fit models and the *SFR* calculated by CIGALE. The Pearson coefficient is 0.81 ($\rho = 0.81$), and the fitted line is log (*SFR*) = −41.55 + 0.98log (L_{PAH}). The equation from Shipley et al. (2016) is also plotted for comparison. The galaxies are colored according to their redshifts: $z <$ 0.5 galaxies are blue, and $z >$ 0.5 galaxies are red. Both local and distant galaxies seem to follow the relation, although there are some outliers. (Color online)

We also calculated the 7.7 μm luminosities from *S11*, *L15*, and *L18* (depending on the redshift of the object), and compared it to L_{IR} from our CIGALE fits (figure 9). We got a similar relation, but our galaxies have systematically lower log [$\nu L_\nu(7.7\,\mu m)$] than we would expect from the relation in Houck et al. (2007).

We also checked that the luminosities from the SEDs were similar to those calculated from the AKARI fluxes ($\rho = 0.96$). We tried to plot q_{PAH} as a function of L_{IR} (figure 7), but could not get a clear correlation like the one between the 7.7 μm luminosities and L_{IR}. We also compared q_{PAH} and log [$\nu L_\nu(7.7\mu m)$]: the correlation coefficient is 0.58. Our L_{IR} values (with 25% relative errors) are more precise than those with 50% relative errors from Takagi et al. (2010), and in the SED fitting we also used photometric points beyond 30 μm.

Murata et al. (2014) examined the $\nu L_8/\nu L_{4.5}$ and $L_{IR}/\nu L_8$ luminosity ratios ($L_{4.5}$ and L_8 are the specific luminosities at 4.5 and 8 μm) as functions of R_{SB}. They assumed that $\nu L_8/\nu L_{4.5}$ corresponds to the strength of PAHs compared to the continuum (because the $L_{4.5}$ luminosity is mainly from the continuum, and L_8 is from the PAH features). They found that the ratio increased with starburstiness, then became constant (or even declined depending on the redshift range).

To compare our results, we plotted q_{PAH} as a function of log R_{SB}, as seen in figure 10. As a comparison to previous works, we also plotted data points from Schreiber et al. (2018), calculating the *SFR* from the L_{IR} given in their article (using Kennicutt 1998). We calculated the mean q_{PAH} values in different R_{SB} bins, but it only increased slightly toward log $R_{SB} = 0$, and then stayed constant. This is not similar to the changes seen in the $\nu L_8/\nu L_{4.5}$ luminosity ratios. We compared the q_{PAH} values to the luminosity ratios calculated from the SEDs, but they only showed a slight correlation ($\rho = 0.65$).

Shipley et al. (2016) determined a correlation between the PAH luminosities ($L_{PAH} = L_{6.2} + L_{7.7} + L_{11.3}$) from Spitzer spectra and the star formation rate:

$$\log(SFR) = -42.56 + \log(L_{PAH}). \quad (5)$$

The PAH luminosities were calculated from the fitted SEDs, and compared with the *SFR* derived by CIGALE (figure 11). The two methods give a similar *SFR*, and a similar relation to equation (5) can be fitted to the *SFR* from CIGALE and the PAH luminosities: log(*SFR*) = −41.55 + 0.98 log(L_{PAH}). They also gave relations between the *SFR* and the different components of L_{PAH} ($L_{6.2}$, $L_{7.7}$, $L_{11.3}$).

Downloaded from https://academic.oup.com/pasj/article-abstract/71/2/27/5274622 by The Library of Chinese Academy of Sciences user on 02 August 2019

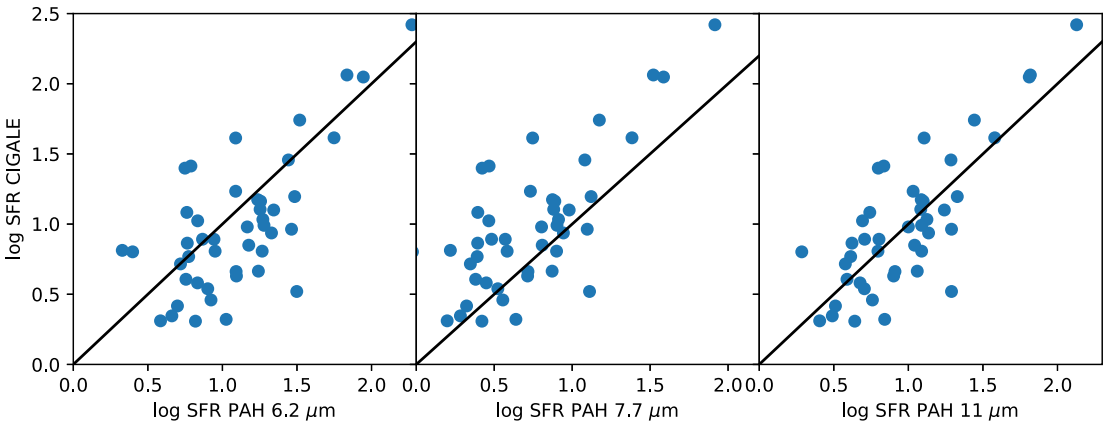


Fig. 12. *SFR* from the 6.2, 7.7, and 11.3 μm luminosities calculated from the SEDs fitted by CIGALE are compared with the *SFR* from CIGALE. The 1-to-1 line is marked in black. The *SFR*s from the different methods have a strong correlation ($\rho = 0.96$). The *SFR* from the 6.2 μm luminosity is usually slightly higher, and the *SFR* from the 7.7 μm luminosity is slightly lower, than the *SFR* from the SED. The *SFR*s from the 11.3 μm luminosities are in good agreement with the *SFR* from the SED. (Color online)

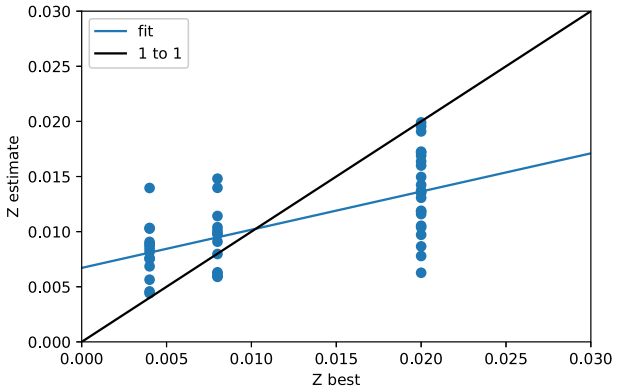


Fig. 13. Result of the mock analysis of the metallicities from CIGALE (the same method as the analysis for $q_{\rm PAH}$, figure 4). Although the relative errors (27%) are similar to the errors of $q_{\rm PAH}$, the mock analysis shows that we cannot estimate the metallicities reliably from our SED fits. (Color online)

We compared the *SFR* from CIGALE with the *SFR* calculated from these luminosities. While the *SFR*s from the 11.3 luminosities were in good agreement with it, the *SFR*s from the 6.2 luminosities seemed to slightly overestimate, and the *SFR*s from the 7.7 luminosities slightly underestimate, the *SFR* from the CIGALE fit (figure 12). We compared the $q_{\rm PAH}$ values to the PAH luminosities calculated from the SEDs, but they only showed a very small correlation ($\rho = 0.4$).

There can be multiple causes for the low $q_{\rm PAH}$ values ($q_{\rm PAH} = 2.04$ on average); one of these is a low metallicity. We tried to derive the metallicities from the SED fits, and even though the relative errors were similar to the errors of the $q_{\rm PAH}$ values (27%), the mock analysis was worse (figure 13). We conclude that we probably cannot estimate the metallicities well enough. But, on average we have metallicities of 0.011.

We also inspected the spectra of the sources with spectroscopic redshifts and $q_{\rm PAH} < 2$ (five galaxies: ID108, ID156, ID261, ID300, ID500). One of them had line ratios similar to AGNs (ID500), which could cause a low $q_{\rm PAH}$. For two galaxies (ID156, ID195), Hα and N II could not have been observed due to their redshifts, so they cannot be classified by the BPT method. One of them (ID108) has a weak O III λ4363 line, which is usually found in low-metallicity galaxies, which could cause low $q_{\rm PAH}$. The model fluxes from SDSS are often very different from the real fluxes of the spectra.

We also checked whether there was a relationship with the attenuation ($A_{\rm V}$, determined from the SED fitting). We found that $q_{\rm PAH}$ and $A_{\rm V}$ were inversely proportional (figure 14), although there is a large dispersion. Galaxies with low $q_{\rm PAH}$ had higher attenuation on average, but there were some galaxies with low attenuation too. This suggests that low PAH emission is partly because of high dust attenuation. High $A_{\rm V}$ can indicate the compactness of star-forming regions, where PAHs can be suppressed (as shown in Elbaz et al. 2011 and Shipley et al. 2016). Therefore the decreasing trend of $q_{\rm PAH}$ with $A_{\rm V}$ could indicate more compact star-forming regions.

6 Conclusion

The James Webb Space Telescope (JWST) rest-frame near-IR and mid-IR performance will provide new and important information on galaxies in the local universe, but also at high redshift. In this range there are several lines that do not suffer much from dust attenuation. One of the main

Downloaded from https://academic.oup.com/pasj/article-abstract/71/2/27/5274622 by The Library of Chinese Academy of Sciences user on 02 August 2019

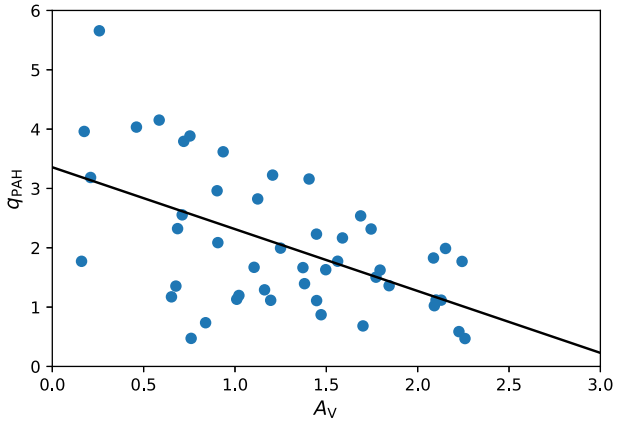


Fig. 14. Value of q_{PAH} compared to the attenuation (A_V). They are inversely proportional, with a correlation coefficient of −0.54. The fitted relation is $q_{PAH} = -1A_V + 3.4$. On average, galaxies with lower q_{PAH} have a higher attenuation, but there are also some cases where both the attenuation and q_{PAH} are low. (Color online)

features that we can study are the PAH emissions. AKARI covered this same wavelength range with a high density of photometric bands. This paper can therefore be considered as a pathfinder to similar studies that will come later from JWST observations.

We determined the main parameters of galaxies with AKARI and Herschel detections at various redshifts (0.04–2.36) in the ELAIS N1 field using CIGALE SED fitting. Our sample was therefore IR-selected, with most of the galaxies in the range $10.5 \leq L_{IR} \leq 11.5$ (78%) and $10.0 \leq M_{star} \leq 11.0$ (82%).

The AKARI mid-IR photometry improved the estimation of q_{PAH}, especially when there were no other photometric points at the wavelengths of the PAH features, or only data with very large errors were available. Including the AKARI data can change the q_{PAH}: in some cases it can be significantly lower or higher than those from SED fitting without AKARI.

The q_{PAH} values usually do not follow the same trends as the PAH luminosities: we found no correlation between q_{PAH} and R_{SB}. There was a weak anti-correlation between q_{PAH} and L_{IR} similar to the trend found in Pope et al. (2013), but opposite to the relation in Houck et al. (2007). The q_{PAH} values only slightly correlated with L_{PAH} and $L_{7.7}$ ($\rho = 0.4$–0.6). On the other hand, we found similar relations to the literature between the PAH luminosities and L_{IR} or the *SFR*. However, $L_{6.2}$ overestimates and $L_{7.7}$ underestimates the *SFR* according to our SED fittings, and we have lower $L_{7.7}$ compared to previous works.

Most of the sources examined had a lower PAH fraction ($q_{PAH} = 2.04$ on average) compared to the literature. There are various possible reasons, and one of these would be high attenuation which could be correlated with the compactness of the star-forming regions. We found that A_V was inversely proportional to q_{PAH}: galaxies in our sample with low q_{PAH} usually also had high A_V. The q_{PAH} values were also below average in low-metallicity galaxies (Ciesla et al. 2014), AGNs, and starbursts (Yamada et al. 2013; Murata et al. 2017). According to our SED fittings, the majority of the sample were near the main sequence of star-forming galaxies, meaning that most of the objects are not starbursts. We have spectroscopic observations only for a fraction of our sources, from which one galaxy could be an AGN and another a low-metallicity galaxy. Our SED fitting accuracy did not allow a reliable determination of metallicity, but further dedicated follow-ups would help.

In order to better understand the lower PAH fraction in our sample of IR-selected galaxies, we need to carry out an extended analysis, using more data. The metallicity dependence of PAH abundance might be due to the strong metallicity dependence of the dust mass increase by the accretion of metals onto dust grains. These dust grains will be shattered into PAHs later in the process. Supernova shock could be the primary mechanism in metal-poor environments leading to PAH destruction (Seok et al. 2014). However, there are still large uncertainties about these various formation/destruction processes. By definition, the IR wavelength range is crucial when dealing with dust characteristics. Here, the main information that we need to secure are the metallicity for our galaxies. For this, we need spectroscopic observations of these objects.

Acknowledgments

This research was supported by the Hungarian OTKA grant NN111016, and by the ÚNKP-18-2 New National Excellence Program of the Ministry of Human Capacities.

This research has made use of the SIMBAD database, and the VizieR catalog access tool, CDS, Strasbourg, France. The original description of the VizieR service was published in Ochsenbein, Bauer, and Marcout (2000).

This publication makes use of data products from the Wide-field Infrared Survey Explorer, which is a joint project of the University of California, Los Angeles, and the Jet Propulsion Laboratory/California Institute of Technology, funded by the National Aeronautics and Space Administration.

Based on observations with AKARI, a JAXA project with the participation of ESA.

Appendix 1. Collected photometry

Downloaded from https://academic.oup.com/pasj/article-abstract/71/2/27/5274622 by The Library of Chinese Academy of Sciences user on 02 August 2019

Table 6. Optical photometry used in the SED fitting.*

ID	u	$u_{\rm err}$	g	$g_{\rm err}$	r	$r_{\rm err}$	i	$i_{\rm err}$	z	$z_{\rm err}$
	354.3		477.0		623.1		762.5		913.4	
5	0.0037	0.0017	0.0037	0.0005	0.0060	0.0008	0.0076	0.0011	0.0140	0.0044
17	0.0013	0.0027	0.0038	0.0007	0.0097	0.0009	0.0152	0.0014	0.0119	0.0061
19	—	—	—	—	—	—	—	—	—	—
23	0.0006	0.0019	0.0005	0.0006	0.0048	0.0008	0.0100	0.0013	0.0109	0.0055
24	0.0024	0.0075	0.0046	0.0015	0.0132	0.0020	0.0165	0.0033	0.0216	0.0150
25	0.0049	0.0023	0.0142	0.0008	0.0376	0.0011	0.0536	0.0017	0.0751	0.0064
47	0.0050	0.0020	0.0053	0.0006	0.0068	0.0008	0.0101	0.0013	0.0144	0.0053
63	0.0534	0.0024	0.1202	0.0011	0.1581	0.0014	0.1817	0.0021	0.2025	0.0069
67	—	—	—	—	—	—	—	—	—	—
68	0.0058	0.0018	0.0036	0.0006	0.0057	0.0008	0.0130	0.0012	0.0105	0.0048
87	0.0038	0.0033	0.0088	0.0010	0.0189	0.0013	0.0314	0.0021	0.0399	0.0083
108	0.0020	0.0025	0.0048	0.0007	0.0114	0.0009	0.0247	0.0014	0.0239	0.0057
111	0.0053	0.0022	0.0063	0.0007	0.0144	0.0010	0.0216	0.0016	0.0315	0.0062
113	0.0034	0.0023	0.0065	0.0007	0.0151	0.0009	0.0245	0.0015	0.0402	0.0058
128	0.0014	0.0027	0.0041	0.0007	0.0120	0.0009	0.0218	0.0014	0.0232	0.0057
140	—	—	—	—	—	—	—	—	—	—
143	0.0002	0.0005	0.0016	0.0006	0.0067	0.0009	0.0095	0.0012	0.0158	0.0049
144	0.0010	0.0049	0.0066	0.0009	0.0163	0.0013	0.0271	0.0020	0.0332	0.0080
156	0.0003	0.0017	0.0006	0.0012	0.0099	0.0013	0.0208	0.0021	0.0409	0.0084
181	0.0008	0.0025	0.0077	0.0007	0.0116	0.0010	0.0211	0.0015	0.0256	0.0054
186	—	—	—	—	—	—	—	—	—	—
191	—	—	—	—	—	—	—	—	—	—
195	0.0014	0.0034	0.0039	0.0008	0.0165	0.0011	0.0500	0.0017	0.0787	0.0064
200	0.0015	0.0037	0.0026	0.0009	0.0074	0.0012	0.0139	0.0019	0.0147	0.0083
215	0.0019	0.0030	0.0049	0.0007	0.0113	0.0010	0.0155	0.0016	0.0128	0.0067
222	0.0071	0.0020	0.0101	0.0007	0.0259	0.0010	0.0308	0.0015	0.0458	0.0054
261	0.0107	0.0023	0.0097	0.0008	0.0207	0.0011	0.0354	0.0018	0.0467	0.0071
264	0.0012	0.0041	0.0057	0.0008	0.0155	0.0012	0.0243	0.0019	0.0563	0.0076
266	0.0048	0.0022	0.0067	0.0007	0.0085	0.0010	0.0135	0.0015	0.0106	0.0065
286	0.0036	0.0025	0.0062	0.0008	0.0243	0.0011	0.0398	0.0017	0.0511	0.0067
289	0.0069	0.0024	0.0220	0.0008	0.0547	0.0012	0.0784	0.0018	0.1025	0.0068
294	0.1971	0.0064	0.6146	0.0031	0.9817	0.0045	1.2787	0.0066	1.4713	0.0216
300	0.0018	0.0034	0.0055	0.0008	0.0078	0.0012	0.0128	0.0017	0.0248	0.0067
305	0.0006	0.0024	0.0035	0.0007	0.0100	0.0009	0.0161	0.0015	0.0091	0.0063
329	0.0063	0.0024	0.0047	0.0008	0.0046	0.0011	0.0098	0.0017	0.0140	0.0070
334	0.1130	0.0056	0.2857	0.0023	0.4370	0.0033	0.5612	0.0051	0.6397	0.0183
347	—	—	—	—	—	—	—	—	—	—
365	0.0095	0.0020	0.0294	0.0007	0.0613	0.0011	0.0865	0.0016	0.1037	0.0055
370	—	—	—	—	—	—	—	—	—	—
385	0.0249	0.0025	0.0758	0.0010	0.1159	0.0015	0.1525	0.0022	0.1686	0.0080
412	0.0001	0.0001	0.0041	0.0007	0.0054	0.0009	0.0026	0.0015	0.0137	0.0057
416	—	—	—	—	—	—	—	—	—	—
417	0.0005	0.0024	0.0027	0.0007	0.0040	0.0010	0.0118	0.0016	0.0215	0.0063
419	0.0076	0.0019	0.0069	0.0006	0.0108	0.0009	0.0138	0.0013	0.0195	0.0055
433	0.0022	0.0041	0.0045	0.0010	0.0029	0.0014	0.0027	0.0025	0.0031	0.0087
438	0.0032	0.0031	0.0045	0.0009	0.0145	0.0012	0.0243	0.0020	0.0250	0.0082
447	0.0031	0.0047	0.0072	0.0012	0.0188	0.0016	0.0305	0.0025	0.0305	0.0107
456	0.0031	0.0051	0.0062	0.0012	0.0177	0.0017	0.0243	0.0027	0.0447	0.0109
490	—	—	—	—	—	—	—	—	—	—
500	0.0039	0.0024	0.0162	0.0008	0.0455	0.0011	0.0683	0.0017	0.0866	0.0063
531	0.0002	0.0002	0.0008	0.0007	0.0054	0.0010	0.0129	0.0015	0.0056	0.0067
545	0.0005	0.0021	0.0026	0.0008	0.0107	0.0010	0.0178	0.0016	0.0419	0.0064
554	0.0002	0.0002	0.0027	0.0004	0.0070	0.0006	0.0111	0.0008	0.0212	0.0033
555	0.0235	0.0022	0.0745	0.0010	0.1501	0.0014	0.2116	0.0021	0.2518	0.0068
559	0.0009	0.0035	0.0042	0.0008	0.0213	0.0011	0.0364	0.0016	0.0554	0.0060
562	0.0058	0.0018	0.0036	0.0006	0.0057	0.0008	0.0130	0.0012	0.0105	0.0048
565	—	—	—	—	—	—	—	—	—	—
568	0.0036	0.0021	0.0040	0.0006	0.0086	0.0008	0.0105	0.0013	0.0173	0.0053
570	0.0008	0.0036	0.0039	0.0009	0.0112	0.0012	0.0179	0.0018	0.0147	0.0078
574	0.0024	0.0024	0.0042	0.0007	0.0135	0.0009	0.0210	0.0014	0.0259	0.0056
580	0.0125	0.0018	0.0122	0.0006	0.0179	0.0008	0.0206	0.0012	0.0189	0.0050
590	0.0137	0.0023	0.0205	0.0008	0.0486	0.0012	0.0626	0.0018	0.0758	0.0071
591	0.0029	0.0104	0.0072	0.0019	0.0261	0.0026	0.0409	0.0041	0.0787	0.0169
597	—	—	—	—	—	—	—	—	—	—

*Fluxes are given in mJy in each filter, and the effective wavelengths below the filters are in nm.

Downloaded from https://academic.oup.com/pasj/article-abstract/71/2/27/5274622 by The Library of Chinese Academy of Sciences user on 02 August 2019

Table 7. Near-infrared photometry of the examined galaxies, up to 4.6 μm.*

ID	WISE1 3.4	WISE1$_{err}$	IRAC1 3.6	IRAC1$_{err}$	*N4* 4.1	*N4*$_{err}$	IRAC2 4.5	IRAC2$_{err}$	WISE2 4.6	WISE2$_{err}$
5	0.030	0.003	—	—	0.009	0.001	—	—	0.030	0.005
17	0.043	0.003	0.040	0.001	0.030	0.002	0.034	0.001	0.032	0.005
19	0.035	0.003	0.043	0.001	0.033	0.003	0.034	0.001	0.029	0.005
23	0.113	0.004	0.103	0.001	0.088	0.004	0.069	0.001	0.082	0.006
24	0.066	0.003	0.060	0.001	0.053	0.003	0.043	0.001	0.050	0.006
25	0.103	0.004	0.079	0.001	0.088	0.004	0.076	0.001	0.090	0.005
47	0.061	0.003	0.065	0.001	0.051	0.003	0.054	0.001	0.049	0.005
63	0.132	0.004	0.102	0.002	0.095	0.004	0.071	0.002	0.080	0.006
67	0.034	0.003	0.026	0.001	0.028	0.002	0.030	0.001	0.026	0.005
68	0.045	0.003	0.047	0.001	0.033	0.003	0.034	0.001	0.020	0.006
87	0.060	0.003	0.051	0.001	0.052	0.003	0.049	0.001	0.049	0.005
108	0.095	0.004	0.083	0.001	0.067	0.004	0.056	0.001	0.048	0.005
111	0.048	0.003	0.041	0.001	0.035	0.003	0.034	0.001	0.027	0.005
113	0.064	0.003	0.057	0.001	0.052	0.003	0.053	0.001	0.053	0.005
128	0.064	0.003	0.061	0.001	0.059	0.003	0.053	0.001	0.047	0.005
140	0.075	0.003	0.067	0.001	0.065	0.004	0.053	0.001	0.043	0.005
143	0.061	0.003	0.060	0.001	0.052	0.003	0.050	0.001	0.049	0.006
144	0.076	0.003	0.059	0.001	0.070	0.004	0.054	0.001	0.058	0.006
156	0.156	0.005	0.124	0.001	0.125	0.005	0.094	0.002	0.111	0.006
181	0.048	0.003	0.035	0.001	0.039	0.003	0.025	0.001	0.034	0.005
186	0.039	0.003	0.041	0.001	0.048	0.003	0.042	0.001	0.053	0.006
191	0.019	0.002	0.027	0.001	0.028	0.002	0.029	0.001	0.013	0.006
195	0.283	0.007	0.173	0.002	0.192	0.006	0.113	0.002	0.176	0.007
200	0.093	0.004	0.078	0.001	0.080	0.004	0.054	0.001	0.074	0.006
215	0.048	0.003	0.035	0.001	0.028	0.002	0.026	0.001	0.036	0.005
222	0.040	0.003	0.033	0.001	0.036	0.003	0.032	0.001	0.034	0.005
261	0.171	0.005	0.120	0.001	0.119	0.005	0.086	0.001	0.107	0.006
264	0.074	0.003	0.066	0.001	0.052	0.003	0.053	0.001	0.037	0.005
266	0.034	0.003	0.020	0.001	0.020	0.002	0.013	0.001	0.015	0.006
286	0.095	0.004	0.073	0.001	0.086	0.004	0.069	0.002	0.080	0.005
289	0.154	0.005	0.126	0.002	0.148	0.005	0.133	0.002	0.125	0.006
294	0.575	0.014	0.971	0.003	0.467	0.011	0.630	0.003	0.377	0.011
300	0.067	0.003	0.071	0.001	0.063	0.004	0.057	0.001	0.046	0.005
305	0.081	0.003	0.058	0.001	0.072	0.004	0.050	0.001	0.061	0.006
329	0.042	0.003	0.042	0.001	0.033	0.003	0.031	0.001	0.018	0.006
334	0.267	0.007	0.471	0.003	0.249	0.007	0.316	0.004	0.186	0.008
347	0.023	0.002	0.028	0.001	0.025	0.002	0.020	0.001	—	—
365	0.103	0.004	0.113	0.001	0.106	0.005	0.095	0.001	0.088	0.006
370	0.019	0.002	0.005	0.000	0.017	0.002	—	—	0.021	0.005
385	0.105	0.004	0.092	0.002	0.094	0.004	0.063	0.002	0.068	0.006
412	0.014	0.003	—	—	0.018	0.002	—	—	0.019	0.006
416	0.069	0.003	0.050	0.001	0.039	0.003	0.036	0.001	0.043	0.005
417	0.069	0.003	0.066	0.001	0.057	0.003	0.051	0.001	0.043	0.005
419	0.081	0.003	0.086	0.001	0.090	0.004	0.073	0.001	0.058	0.005
433	0.017	0.003	—	—	0.030	0.002	—	—	0.025	0.005
438	0.051	0.003	—	—	0.053	0.003	—	—	0.048	0.005
447	0.058	0.003	0.037	0.001	0.050	0.003	0.027	0.001	0.046	0.005
456	0.052	0.003	0.041	0.001	0.039	0.003	0.030	0.001	0.030	0.005
490	0.042	0.003	0.041	0.001	0.033	0.003	0.034	0.001	0.030	0.005
500	0.330	0.009	0.216	0.002	0.306	0.008	0.215	0.002	0.293	0.009
531	0.107	0.004	0.103	0.002	0.083	0.004	0.074	0.002	0.052	0.006
545	0.044	0.003	0.042	0.001	0.020	0.002	0.043	0.001	0.045	0.005
554	0.083	0.003	—	—	—	—	—	—	0.057	0.005
555	0.264	0.007	0.275	0.002	—	—	0.230	0.002	0.226	0.008
559	0.129	0.004	0.108	0.002	—	—	0.096	0.002	0.090	0.006
562	0.045	0.003	0.047	0.001	—	—	0.034	0.001	0.020	0.006
565	0.245	0.007	0.031	0.001	—	—	0.026	0.001	0.166	0.007
568	0.115	0.004	—	—	—	—	—	—	0.066	0.005
570	0.120	0.004	0.050	0.001	—	—	0.038	0.001	0.061	0.005
574	0.065	0.003	0.059	0.001	—	—	0.050	0.001	0.052	0.005
580	0.102	0.004	0.095	0.001	—	—	0.106	0.002	0.122	0.007
590	0.082	0.003	0.063	0.001	—	—	0.059	0.001	0.066	0.005
591	0.106	0.004	0.082	0.001	—	—	0.059	0.001	0.063	0.006
597	0.037	0.003	0.034	0.001	—	—	0.032	0.001	0.029	0.005

*Fluxes are in mJy, and the effective wavelengths below the filters are in μm.

Downloaded from https://academic.oup.com/pasj/article-abstract/71/2/27/5274622 by The Library of Chinese Academy of Sciences user on 02 August 2019

Table 8. Mid-infrared photometry of the examined galaxies from 5.8 μm to 15 μm.*

ID	IRAC3 5.8	IRAC3$_{err}$	IRAC4 8.	IRAC4$_{err}$	*S11* 11.	*S11*$_{err}$	WISE3 12.	WISE3$_{err}$	*L15* 15.	*L15*$_{err}$
5	—	—	—	—	0.14	0.01	—	—	—	—
17	—	—	—	—	—	—	0.14	0.07	0.11	0.02
19	0.04	0.00	—	—	—	—	0.16	0.08	0.29	0.02
23	0.06	0.00	0.05	0.00	0.13	0.01	0.13	0.08	0.16	0.02
24	—	—	—	—	—	—	0.14	0.08	0.28	0.02
25	—	—	0.14	0.00	—	—	0.29	0.06	0.27	0.02
47	0.06	0.00	0.04	0.00	0.13	0.01	—	—	0.17	0.02
63	0.07	0.01	0.24	0.01	0.23	0.01	0.20	0.07	0.27	0.02
67	—	—	—	—	—	—	0.18	0.07	—	—
68	0.05	0.00	0.03	0.00	—	—	0.37	0.07	—	—
87	0.04	0.00	0.07	0.00	0.23	0.01	0.25	0.07	0.23	0.02
108	0.07	0.00	0.06	0.01	0.08	0.01	0.24	0.07	0.25	0.02
111	0.04	0.00	—	—	0.10	0.01	0.14	0.07	—	—
113	0.05	0.00	0.10	0.01	0.30	0.01	0.36	0.07	0.30	0.02
128	—	—	0.08	0.00	0.08	0.01	0.18	0.08	—	—
140	0.03	0.00	0.06	0.00	0.11	0.01	—	—	0.09	0.01
143	0.05	0.00	0.06	0.00	0.21	0.01	0.20	0.07	—	—
144	—	—	0.09	0.01	0.10	0.01	0.25	0.07	0.25	0.02
156	0.09	0.00	0.10	0.01	0.32	0.01	0.23	0.07	0.23	0.02
181	0.04	0.00	—	—	—	—	0.19	0.08	0.21	0.02
186	0.04	0.00	—	—	—	—	—	—	—	—
191	—	—	—	—	—	—	—	—	0.15	0.02
195	0.09	0.00	—	—	0.25	0.01	0.25	0.07	0.32	0.02
200	—	—	—	—	—	—	0.21	0.07	0.19	0.02
215	—	—	—	—	—	—	—	—	—	—
222	—	—	0.06	0.00	0.08	0.01	—	—	—	—
261	0.06	0.00	0.07	0.00	0.22	0.01	0.45	0.07	0.58	0.03
264	0.05	0.00	0.06	0.01	0.26	0.01	0.22	0.07	0.22	0.02
266	—	—	—	—	—	—	0.16	0.08	0.17	0.02
286	0.05	0.00	0.12	0.01	0.43	0.01	0.31	0.07	0.37	0.02
289	0.08	0.01	0.34	0.01	0.83	0.02	0.68	0.07	0.70	0.03
294	0.75	0.01	2.59	0.01	1.72	0.02	1.70	0.08	1.45	0.04
300	—	—	—	—	0.10	0.01	0.24	0.08	0.50	0.02
305	0.04	0.00	0.05	0.00	0.22	0.01	0.21	0.08	0.16	0.02
329	0.03	0.00	—	—	—	—	—	—	0.15	0.02
334	0.34	0.01	1.63	0.01	1.14	0.02	1.11	0.08	1.03	0.03
347	—	—	—	—	—	—	0.14	0.08	—	—
365	0.08	0.00	0.36	0.01	0.43	0.01	0.45	0.07	0.50	0.02
370	—	—	—	—	—	—	—	—	0.15	0.02
385	0.05	0.00	0.33	0.01	0.26	0.01	0.36	0.07	0.33	0.02
412	—	—	—	—	—	—	—	—	0.15	0.02
416	—	—	—	—	0.21	0.01	0.22	0.07	—	—
417	—	—	0.05	0.00	—	—	0.22	0.07	0.37	0.02
419	0.08	0.01	0.10	0.00	0.15	0.01	0.18	0.08	0.28	0.02
433	—	—	—	—	0.07	0.01	—	—	0.15	0.02
438	—	—	—	—	0.08	0.01	—	—	—	—
447	—	—	—	—	0.17	0.01	0.19	0.07	0.20	0.02
456	—	—	—	—	—	—	—	—	0.17	0.02
490	—	—	—	—	—	—	0.26	0.07	0.25	0.02
500	0.18	0.01	0.98	0.01	1.35	0.02	1.39	0.08	1.28	0.04
531	0.10	0.01	0.06	0.01	0.18	0.01	0.31	0.07	0.24	0.02
545	—	—	0.12	0.00	0.11	0.01	0.26	0.07	—	—
554	—	—	—	—	0.21	0.01	0.12	0.08	—	—
555	0.19	0.01	1.58	0.01	0.69	0.01	1.73	0.09	1.39	0.04
559	0.06	0.01	0.11	0.01	0.22	0.01	0.26	0.08	—	—
562	0.05	0.00	0.03	0.00	0.23	0.01	0.37	0.07	—	—
565	—	—	—	—	0.19	0.01	0.21	0.07	0.30	0.02
568	—	—	—	—	0.15	0.01	—	—	—	—
570	—	—	—	—	0.11	0.01	—	—	0.11	0.02
574	—	—	0.07	0.01	—	—	0.32	0.07	0.31	0.02
580	0.13	0.01	0.15	0.01	—	—	0.26	0.07	0.61	0.03
590	0.04	0.00	0.14	0.00	—	—	0.17	0.08	—	—
591	0.06	0.00	0.04	0.00	—	—	0.22	0.07	—	—
597	—	—	0.04	0.00	—	—	0.18	0.07	—	—

*Fluxes are in mJy, and the effective wavelengths below the filters are in μm.

Downloaded from https://academic.oup.com/pasj/article-abstract/71/2/27/5274622 by The Library of Chinese Academy of Sciences user on 02 August 2019

Table 9. Mid- to far-infrared photometry of the examined galaxies from 18 to 100 μm.*

ID	*L18W* 18.	$L18W_{\rm err}$	WISE4 22.	$WISE4_{\rm err}$	MIPS1 24.	$MIPS1_{\rm err}$	MIPS2 100.	$MIPS2_{\rm err}$	PACS *g* 100.	PACS $g_{\rm err}$
5	0.18	0.02	—	—	—	—	—	—	—	—
17	0.20	0.02	—	—	0.19	0.02	—	—	—	—
19	0.42	0.02	—	—	0.48	0.02	—	—	—	—
23	0.30	0.02	1.08	0.56	0.37	0.01	—	—	—	—
24	0.26	0.02	1.25	0.56	0.42	0.01	—	—	—	—
25	0.40	0.02	—	—	0.38	0.01	—	—	—	—
47	0.18	0.02	—	—	0.29	0.01	—	—	—	—
63	0.23	0.02	—	—	0.51	0.02	11.10	3.09	—	—
67	0.36	0.02	—	—	0.20	0.02	—	—	—	—
68	0.43	0.02	1.01	0.61	0.61	0.02	13.80	3.00	—	—
87	0.23	0.02	—	—	0.38	0.02	—	—	—	—
108	0.25	0.02	—	—	0.44	0.02	—	—	—	—
111	—	—	—	—	0.16	0.02	—	—	—	—
113	0.35	0.02	—	—	0.49	0.02	—	—	—	—
128	0.21	0.02	—	—	0.21	0.01	—	—	—	—
140	—	—	—	—	0.28	0.02	—	—	—	—
143	0.23	0.02	—	—	0.22	0.02	—	—	—	—
144	0.28	0.02	—	—	0.24	0.01	—	—	—	—
156	0.40	0.02	—	—	0.46	0.02	—	—	—	—
181	0.39	0.02	—	—	—	—	—	—	—	—
186	0.12	0.02	—	—	—	—	—	—	—	—
191	0.25	0.02	—	—	0.19	0.02	—	—	—	—
195	0.26	0.02	—	—	—	—	—	—	—	—
200	0.19	0.02	—	—	0.25	0.02	—	—	—	—
215	0.17	0.02	0.97	0.61	—	—	—	—	—	—
222	—	—	—	—	—	—	—	—	—	—
261	0.61	0.02	—	—	0.69	0.01	—	—	—	—
264	0.43	0.02	1.08	0.62	0.30	0.02	—	—	—	—
266	—	—	—	—	0.17	0.02	—	—	—	—
286	0.62	0.02	—	—	0.30	0.02	—	—	—	—
289	0.86	0.03	1.58	0.57	0.86	0.02	9.50	2.97	—	—
294	1.24	0.03	1.71	0.54	1.33	0.02	16.80	2.71	—	—
300	0.54	0.02	—	—	0.89	0.02	—	—	—	—
305	0.11	0.02	—	—	0.21	0.02	—	—	—	—
329	0.14	0.02	—	—	0.30	0.01	—	—	—	—
334	1.22	0.03	1.45	0.59	1.11	0.02	25.70	2.92	—	—
347	0.14	0.02	—	—	0.25	0.02	—	—	—	—
365	0.37	0.02	0.95	0.60	0.54	0.02	—	—	—	—
370	—	—	—	—	—	—	—	—	—	—
385	0.25	0.02	—	—	0.28	0.01	—	—	—	—
412	0.21	0.02	—	—	—	—	—	—	—	—
416	—	—	—	—	0.27	0.02	—	—	—	—
417	—	—	—	—	0.41	0.02	—	—	—	—
419	0.41	0.02	—	—	0.43	0.02	—	—	—	—
433	0.23	0.02	—	—	—	—	—	—	—	—
438	0.18	0.02	—	—	—	—	—	—	—	—
447	0.17	0.02	—	—	0.24	0.02	—	—	—	—
456	0.18	0.02	—	—	0.17	0.01	—	—	—	—
490	0.29	0.02	1.04	0.63	0.37	0.02	—	—	—	—
500	1.43	0.03	2.05	0.54	1.59	0.02	52.90	2.77	112.66	11.53
531	0.25	0.02	—	—	0.44	0.01	—	—	—	—
545	0.18	0.02	—	—	0.26	0.02	—	—	—	—
554	—	—	—	—	—	—	—	—	—	—
555	2.32	0.04	4.17	0.53	4.02	0.02	38.30	3.27	—	—
559	—	—	—	—	0.31	0.02	—	—	—	—
562	—	—	1.01	0.61	0.61	0.02	13.80	3.00	—	—
565	0.31	0.02	—	—	0.12	0.01	—	—	—	—
568	—	—	—	—	—	—	—	—	—	—
570	0.11	0.02	—	—	—	—	—	—	—	—
574	0.30	0.02	—	—	0.32	0.02	—	—	—	—
580	0.73	0.03	—	—	0.56	0.01	—	—	—	—
590	0.45	0.02	—	—	0.30	0.02	—	—	—	—
591	0.27	0.02	—	—	0.23	0.01	—	—	—	—
597	0.25	0.01	—	—	0.18	0.02	—	—	—	—

*Fluxes are in mJy, and the effective wavelengths below the filters are in μm.

Downloaded from https://academic.oup.com/pasj/article-abstract/71/2/27/5274622 by The Library of Chinese Academy of Sciences user on 02 August 2019

Table 10. Far-infrared photometry of the examined galaxies, from 160 to 500 μm.*

ID	MIPS3 160	MIPS3$_{err}$	PACS r 160	PACS r_{err}	PSW 250	PSW$_{err}$	PMW 350	PMW$_{err}$	PLW 500	PLW$_{err}$
5	—	—	—	—	10.24	2.87	—	—	—	—
17	—	—	—	—	11.27	2.93	—	—	—	—
19	—	—	—	—	11.27	2.93	—	—	—	3.17
23	—	—	—	—	—	—	—	—	18.70	1.90
24	—	—	—	—	19.30	1.70	—	—	—	—
25	—	—	—	—	15.20	1.70	14.22	2.27	—	—
47	—	—	85.51	14.41	—	—	—	—	—	—
63	—	—	—	—	13.14	2.77	9.76	2.32	—	—
67	—	—	—	—	22.50	1.60	24.32	2.24	—	—
68	—	—	—	—	—	—	—	—	9.56	3.02
87	—	—	—	—	35.10	1.60	41.60	1.60	32.70	2.00
108	—	—	—	—	14.50	1.70	9.03	2.32	12.60	2.74
111	—	—	—	—	24.07	2.65	16.72	2.28	—	—
113	—	—	—	—	22.99	7.40	—	—	—	—
128	—	—	—	—	22.30	1.60	—	—	—	—
140	—	—	—	—	—	—	11.33	2.33	—	—
143	—	—	—	—	22.10	1.70	16.16	2.31	9.56	3.02
144	—	—	—	—	—	—	10.02	2.33	—	—
156	—	—	—	—	17.80	1.70	—	—	—	—
181	—	—	—	—	26.50	1.60	30.20	1.60	25.00	1.90
186	—	—	—	—	12.04	2.80	11.54	2.34	—	—
191	—	—	—	—	13.67	2.71	—	—	—	—
195	—	—	—	—	17.80	1.70	—	—	—	—
200	—	—	—	—	39.60	1.60	36.80	1.60	21.40	2.00
215	—	—	—	—	—	—	13.38	2.33	17.29	2.82
222	—	—	—	—	21.37	2.62	—	—	—	—
261	—	—	—	—	29.10	1.60	16.20	1.60	—	—
264	—	—	—	—	14.02	2.84	—	—	—	—
266	—	—	—	—	13.38	2.78	10.80	2.26	—	—
286	—	—	—	—	29.30	1.60	17.63	2.22	—	—
289	—	—	66.82	15.76	25.90	1.60	—	—	—	—
294	115.80	4.67	125.04	16.63	63.40	1.60	—	—	—	—
300	—	—	—	—	21.25	2.75	—	—	—	—
305	—	—	—	—	9.06	2.82	—	—	—	—
329	—	—	—	—	18.40	1.70	—	—	33.30	1.90
334	—	—	81.82	15.63	46.50	1.50	38.00	1.60	38.20	2.10
347	—	—	—	—	13.27	2.80	—	—	12.68	3.04
365	—	—	—	—	14.68	2.61	—	—	—	—
370	—	—	—	—	11.48	2.96	11.07	2.32	—	—
385	—	—	—	—	15.70	1.70	19.20	1.70	—	—
412	—	—	—	—	14.50	2.75	—	—	—	—
416	—	—	—	—	18.43	2.69	—	—	—	—
417	—	—	—	—	—	2.69	13.47	2.32	—	—
419	—	—	—	—	—	—	—	—	14.34	3.01
433	—	—	—	—	15.30	2.76	18.56	2.11	—	—
438	—	—	—	—	22.90	1.70	27.20	1.60	19.50	1.90
447	—	—	—	—	10.80	2.75	—	—	—	—
456	—	—	—	—	—	—	—	—	9.10	2.95
490	—	—	—	—	11.66	2.86	—	—	—	—
500	187.20	5.92	146.89	17.52	90.60	1.60	42.80	1.60	47.70	1.90
531	—	—	—	—	15.50	1.70	—	—	—	—
545	—	—	—	—	9.61	2.84	—	—	—	—
554	—	—	—	—	—	—	—	—	12.87	3.10
555	—	—	120.68	18.66	23.30	1.60	—	—	—	—
559	—	—	76.05	17.63	30.70	1.60	28.40	1.60	18.40	2.10
562	—	—	—	—	22.50	1.60	24.32	2.24	9.56	3.02
565	—	—	—	—	22.30	1.60	—	—	—	—
568	—	—	—	—	—	—	17.56	2.33	—	—
570	—	—	—	—	—	—	17.63	2.22	—	—
574	—	—	—	—	17.40	1.70	24.90	1.50	20.70	2.00
580	—	—	—	—	29.10	1.60	26.50	1.60	17.00	2.10
590	—	—	—	—	12.24	2.86	—	—	—	—
591	—	—	—	—	16.50	1.70	14.84	2.38	—	—
597	—	—	—	—	15.20	1.70	10.99	2.25	—	—

*Fluxes are in mJy, and the effective wavelengths below the filters are in μm.

Downloaded from https://academic.oup.com/pasj/article-abstract/71/2/27/5274622 by The Library of Chinese Academy of Sciences user on 02 August 2019

References

Abolfathi, B., et al. 2018, ApJS, 235, 42
Aniano, G., et al. 2012, ApJ, 756, 138
Baldwin, J. A., Phillips, M. M., & Terlevich, R. 1981, PASP, 93, 5
Blanton, M. R., et al. 2017, AJ, 154, 28
Boquien, M., Burgarella, D., Roehlly, Y., Buat, V., Ciesla, L., Corre, D., Inoue, A. K., & Salas, H. 2018, arXiv:1811.03094
Brandl, B. R., et al. 2006, ApJ, 653, 1129
Bruzual, G., & Charlot, S. 2003, MNRAS, 344, 1000
Burgarella, D., Buat, V., & Iglesias-Páramo, J. 2005, MNRAS, 360, 1413
Caputi, K. I., et al. 2007, ApJ, 660, 97
Chabrier, G. 2003, PASP, 115, 763
Ciesla, L., et al. 2014, A&A, 565, A128
Croft, S., Bower, G. C., & Whysong, D. 2013, ApJ, 762, 93
Cutri, R. M., et al. 2014, VizieR Online Data Catalog, II/328
Davidge, H., Serjeant, S., Pearson, C., Matsuhara, H., Wada, T., Dryer, B., & Barrufet, L. 2017, MNRAS, 472, 4259
Draine, B. T., & Li, A. 2007, ApJ, 657, 810
Elbaz, D., et al. 2011, A&A, 533, A119
Giovannoli, E., Buat, V., Noll, S., Burgarella, D., & Magnelli, B. 2011, A&A, 525, A150
Grant, J. K., Taylor, A. R., Stil, J. M., Landecker, T. L., Kothes, R., Ransom, R. R., & Scott, D. 2010, ApJ, 714, 1689
Herschel Science Ground Segment, Consortium 2011, Astrophysics Source Code Library, ascl:1111.001
Houck, J. R., Weedman, D. W., Le Floc'h, E., & Hao, L. 2007, ApJ, 671, 323
Ishihara, D., et al. 2010, A&A, 514, A1
Kennicutt, R. C., Jr. 1998, ARA&A, 36, 189
Marton, G., et al. 2017, arXiv:1705.05693
Mathis, J. S., Mezger, P. G., & Panagia, N. 1983, A&A, 128, 212
Murakami, H., et al. 2007, PASJ, 59, S369
Murata, K., et al. 2014, A&A, 566, A136
Murata, K. L., Yamada, R., Oyabu, S., Kaneda, H., Ishihara, D., Yamagishi, M., Kokusho, T., & Takeuchi, T. T. 2017, MNRAS, 472, 39
Noeske, K. G., et al. 2007, ApJ, 660, L43
Noll, S., Burgarella, D., Giovannoli, E., Buat, V., Marcillac, D., & Muñoz-Mateos, J. C. 2009, A&A, 507, 1793
Ochsenbein, F., Bauer, P., & Marcout, J. 2000, A&AS, 143, 23
Oliver, S., et al. 2000, MNRAS, 316, 749
Onaka, T., et al. 2007, PASJ, 59, S401
Peeters, E., Spoon, H. W. W., & Tielens, A. G. G. M. 2004, ApJ, 613, 986
Pilbratt, G. L., et al. 2010, A&A, 518, L1
Pope, A., et al. 2013, ApJ, 772, 92
Rodighiero, G., et al. 2011, ApJ, 739, L40
Roehlly, Y., Burgarella, D., Buat, V., Boquien, M., Ciesla, L., & Heinis, S. 2014, in ASP Conf. Ser., 485, Astronomical Data Analysis Software and Systems XXIII, ed. N. Manset & P. Forshay (San Francisco: ASP), 347
Rowan-Robinson, M., et al. 1999, The Universe as Seen by ISO, ed. P. Cox & M. F. Kessler, ESA-SP 427 (Noordwijk: ESA), 1011
Rowan-Robinson, M., Gonzalez-Solares, E., Vaccari, M., & Marchetti, L. 2013, MNRAS, 428, 1958
Sargent, M. T., Béthermin, M., Daddi, E., & Elbaz, D. 2012, ApJ, 747, L31
Schreiber, C., et al. 2015, A&A, 575, A74
Schreiber, C., Elbaz, D., Pannella, M., Ciesla, L., Wang, T., & Franco, M. 2018, A&A, 609, A30
Schulz, B., et al. 2017, arXiv:1706.00448
Seok, J. Y., Hirashita, H., & Asano, R. S. 2014, MNRAS, 439, 2186
Shipley, H. V., Papovich, C., Rieke, G. H., Brown, M. J. I., & Moustakas, J. 2016, ApJ, 818, 60
Takagi, T., et al. 2007, PASJ, 59, S557
Takagi, T., et al. 2010, A&A, 514, A5
Tielens, A. G. G. M. 2008, ARA&A, 46, 289
Veilleux, S., & Osterbrock, D. E. 1987, ApJS, 63, 295
Weedman, D. W., et al. 2005, ApJ, 633, 706
Yamada, R., Oyabu, S., Kaneda, H., Yamagishi, M., Ishihara, D., Kim, J. H., & Im, M. 2013, PASJ, 65, 103

Downloaded from https://academic.oup.com/pasj/article-abstract/71/2/27/5274622 by The Library of Chinese Academy of Sciences user on 02 August 2019